# Divertor of the European DEMO: Engineering and technologies for power exhaust

J.H. You[1]*, G. Mazzone[2], E. Visca[2], H. Greuner[1], M. Fursdon[3], Y. Addab[4], C. Bachmann[5], T. Barrett[3], U. Bonavolontà[6, a], B. Böswirth[1], F.M. Castrovinci[7], C. Carelli[3], D. Coccorese[6], R. Coppola[8], F. Crescenzi[2], G. Di Gironimo[6], P.A. Di Maio[7], G. Di Mambro[9], F. Domptail[3], D. Dongiovanni[2], G. Dose[10], D. Flammini[2], L. Forest[11], P. Frosi[2], F. Gallay[4, b], B-E. Ghidersa[12], C. Harrington[3], K. Hunger[1], V. Imbriani[6], M. Li[1, c], A. Lukenskas[3, d], A. Maffucci[9], N. Mantel[3], D. Marzullo[13], T. Minniti[3], A. v. Müller[1], S. Noce[10], M.T. Porfiri[2], A. Quartararo[7], M. Richou[4], S. Roccella[2], D. Terentyev[14], A. Tincani[15], E. Vallone[7], S. Ventre[9], R. Villari[2], F. Villone[16], C. Vorpahl[5], K. Zhang[1]

[1] Max Planck Institute for Plasma Physics, Boltzmannstr. 2, 85748 Garching, Germany
[2] ENEA Frascati, Dept. of Fusion and Technology for Nuclear Safety, via E. Fermi 45, 00044 Frascati, Italy
[3] CCFE, Culham Science Centre, Abingdon OX14 3DB, United Kingdom
[4] CEA, IRFM, F-13108 Saint Paul Lez Durance, France
[5] EUROfusion PMU, Dept. of PPPT, Boltzmann Str. 2, 85748 Garching, Germany
[6] CREATE/Univ. of Naples, Dept. of Industrial Engineering, Piazzale Tecchio 80, 80125 Napoli, Italy
[7] Univ. of Palermo, Dept. of Engineering, Viale delle Scienze, Building 6, 90128 Palermo, Italy
[8] ENEA Casaccia, Dept. of Fusion and Nuclear Safety, Via Anguillarese 301, 00123 Roma, Italy
[9] CREATE/Univ. of Cassino and Southern Lazio, Via G. Di Biasio 43, 03043 Cassino, Italy
[10] Univ. of Rom Tor Vergata, Dept. of Industrial Engineering, Via del Politecnico 1, 00133 Rom, Italy
[11] CEA, DEN-SEMT, Univ. of Paris-Saclay, F-91191 Gif sur Yvette, France
[12] KIT, IAM, Hermann-von-Helmholtz-Platz 1, 76344 Eggenstein-Leopoldshafen, Germany
[13] Univ. of Trieste, Dept. of Engineering, Via Alfonso Valerio, 6/1, 34127, Trieste, Italy
[14] SCK CEN, Institute for Nuclear Materials Science, Mol, 2400, Belgium
[15] ENEA Brasimone, Località Brasimone, 40032 Camugnano Bologna, Italy
[16] University of Naples, Dept. of Electrical Engineering, Via Claudio 21, 80125 Naples, Italy

*a*) currently, NIER Ingegneria, b) ENGIE, c) OSRAM Opto Semiconductors, d) ITER IO

*Corresponding author: Jeong-Ha You (you@ipp.mpg.de)
Phone: +49 89 3299 1373, Fax: +49 89 3299 1212

## Abstract

In a power plant scale fusion reactor, a huge amount of thermal power produced by the fusion reaction and external heating must be exhausted through the narrow area of the divertor targets. The targets must withstand the intense bombardment of the diverted particles where high heat fluxes are generated and erosion takes place on the surface. A considerable amount of volumetric nuclear heating power must also be exhausted. To cope with such an unprecedented power exhaust challenge, a highly efficient cooling capacity is required. Furthermore, the divertor must fulfil other critical functions such as nuclear shielding and channeling (and compression) of exhaust gas for pumping. Assuring the structural integrity of the neutron-irradiated (thus embrittled) components is a crucial prerequisite for a reliable operation over the lifetime. Safety, maintainability, availability, waste and costs are another points of consideration.
In late 2020, the Pre-Conceptual Design activities to develop the divertor of the European demonstration fusion reactor were officially concluded. On this occasion, the baseline design and the key technology options were identified and verified by the project team (EUROfusion Work Package Divertor) based on seven years of R&D efforts and endorsed by Gate Review Panel.
In this paper, an overview of the load specifications, brief descriptions of the design and the highlights of the technology R&D work are presented together with the further work still needed.

Key words: DEMO, Fusion reactor, Divertor, Plasma-facing component, High-heat-flux, Power exhaust

## 1. Introduction

In late 2020, the Pre-Concept Design (PCD) Phase of the European DEMO fusion reactor (that will be simply called DEMO in the rest of the paper) that were started in 2014 [1, 2] were concluded. A dedicated work package (WPDIV) was installed to develop the divertor of the DEMO. The final design review and the gate review endorsed the baseline design and the key technology options. The aim of this paper is to present the outcome of the work conducted in the PCD Phase including the latest technology achievements. Further information, on design options that were considered in the initial design phase can also be found in [3-6].

### 1.1 Functions, high-level requirements and configuration

The divertor in a fusion reactor based on the diverted plasma concept (such as ITER or DEMO) is a key in-vessel component and carries out critical functions as follows [7-10]:

1) To block the plasma particles flowing in the scrape-off layer (SOL)
2) To form gas flow channels and baffles towards pumping ports for exhausting unburnt deuterium-tritium (D-T) fuel and helium 'ash'
3) To remove heat produced by particle bombardment, radiation and volumetric nuclear heating
4) To shield the vacuum vessel (VV) and magnets against nuclear loads
5) To provide physically compatible surface to plasma (high Z, refractory, low tritium retention, etc.)

In the DEMO, the divertor shall be subjected to very harsh loading environment, but is supposed to operate reliably for the envisaged lifetime. Furthermore, there are several high-level requirements which should be considered as fundamental engineering constraints and design drivers, namely [11]:

1) To minimize the nuclear waste from replaced divertor components (particularly, intermediate level[1])
2) To pursue reasonable manufacturing costs and maximal recycling potential
3) To minimize design complexity for reducing maintenance downtime.

Fig. 1 shows the CAD model of the DEMO (2020 version) illustrating the 3D architecture with the single null divertor configuration. The current baseline configuration adopted for the DEMO is the so-called 'single-null' divertor concept where the divertor is located at the bottom of the VV [1]. The SOL field lines intersect the targets.

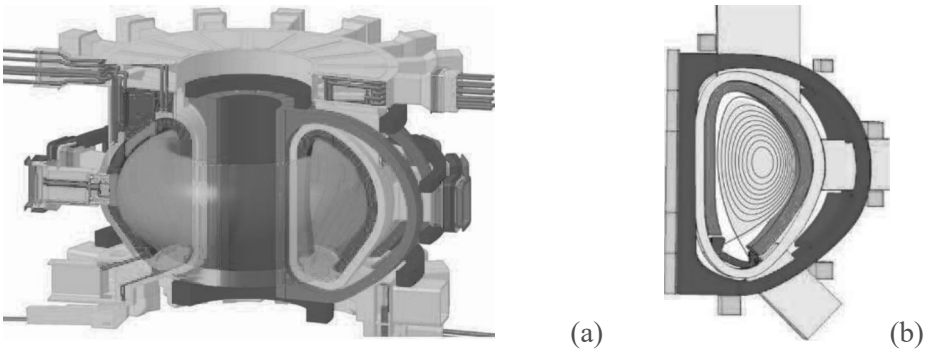

(a) (b)

Fig. 1. CAD configuration model of the European DEMO showing the internal cut view (a) and the poloidal magnetic configuration adapted from [12] (b).

The DEMO divertor currently consists of 48 separate cassette modules arrayed along the toroidal direction. Each cassette module shall be deployed or retracted via an associated lower port for installation and maintenance [13]. Each module comprises following components [14, 15]:

1) Two target plates on which the impinging SOL particles are stopped

[1] The design rules of DEMO foresee no materials which can transmute to high level waste.

2) Cassette body which holds the targets and other shielding components
3) Shielding components (shielding liner and reflector plates) which protects the VV and pipes
4) Pipework of the cooling circuits

### 1.2 Particle exhaust and power exhaust

For a stable fusion operation, the concentration of the helium ash accumulating in the burning plasma must be controlled below the dilution threshold. This control is achieved by the diverted magnetic configuration (see Fig. 2). In this configuration, the plasma particles (fuel/ash mixture) drift outwards, enter into the SOL crossing the separatrix at the plasma edge and are guided along the SOL towards the divertor targets where they are eventually stopped, neutralized and pumped out together with impurities [16].

When impinging upon the target surface, the energetic particles transfer thermal power producing high heat fluxes. In this way, a substantial fraction of the fusion power (carried by alpha particles) and the auxiliary heating power (carried by the fuel plasma) is transported to the divertor targets via the SOL. This thermal power must be exhausted at the targets by means of active cooling to enable a long-pulse operation. As the thickness of the SOL is small, the thermal power density is concentrated on a narrow band (strike point) of the targets leading to a local heat flux peaking. The key plasma parameters of the DEMO related to power exhaust are summarized in Table 1 [17-19]. For comparison, the values of ITER are also given. The near-SOL (characteristic scrape-off length $\lambda_q \cong$ 1mm) thermal power carried by the charged particles reaches 31MW at the SOL radiation fraction of 70%), which can produce exceedingly high heat fluxes (HHF) at the strike point on the targets (power density: ≥10MW/m²). At a lower SOL radiation fraction, the particle power becomes accordingly higher (e.g. 69MW at 40%). This situation raises the critical issue of power handling, a serious physical and technological challenge commonly confronted in the designing of a large-scale (GW range) fusion reactor.

Table 1. Key plasma parameters of the European DEMO and ITER related to power exhaust [19].

| Parameters | EU-DEMO | ITER |
|---|---|---|
| Pulse (s) | 7200 | 400 |
| $R_p/a_p$ (m) | 9.0/2.9 | 6.2/2.0 |
| $q_{95}$ | 3.5 | 3 |
| $\beta_N$ | 2.6 | 1.8 |
| $f_{GW}$ (= $n_e/n_{GW}$) | 1.2 | 0.83 |
| $P_{fusion}$ ($MW_{th}$) | 2000 | 500 |
| $P_{el}$ ($MW_e$) | 500 | - |
| $P_{aux}$ (MW) | 50 | 73 (capacity) |
| $P_{heat}$ (= $P_\alpha + P_{aux}$) (MW) | 457 | 173 |
| Q | 41 | 5/10 |
| $c_{imp,\ core}$ (= $n_{imp}/n_e$) | 0.039 (Xe) + Ar | $N_2$, Ne, Ar |
| $P_{rad,\ core}$ (MW) | 306 | ~50 |
| $f_{rad,\ core}$ (= $P_{rad,\ core}/P_{heat}$) (MW) | 0.67 | ~0.33 |
| $P_{sep}$ (MW) | 154 | ~100 |
| $P_{sep}/R_p$ (MW/m) | 17 | ~16 |
| $P_{L\text{-}H\ th}$ (MW) | 133MW | ~84 |
| $f_{L\text{-}H\ th}$ (= $P_{sep}/P_{L\text{-}H\ th}$) | 1.2 | ~1.2 |

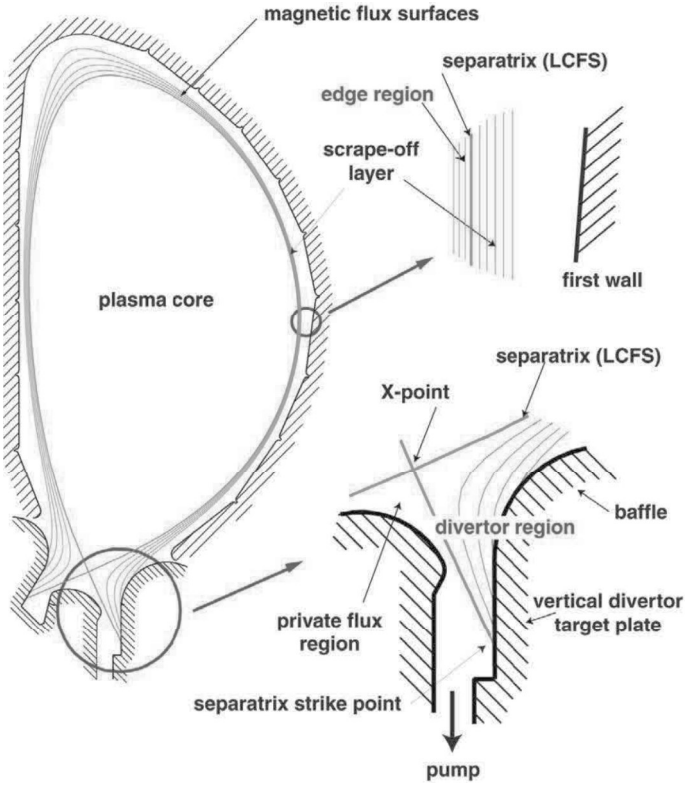


Fig. 2. Schematic illustration of the generic magnetic field profiles in the edge layer of a typical tokamak with the diverted magnetic configuration (poloidal cut section) [11]. (Courtesy from IoP/IAEA)

For mitigating the power density concentration to an acceptable level, two approaches are employed:

1) Inclined targets at a shallow angle (2-3°) relative to the grazing magnetic field lines to expand the footprint of the magnetic field flux on the targets so that the wetted area is increased [7].
2) Power dissipation by means of radiative cooling in the SOL and in the proximity of the targets using seeded inert gas (injected below the allowable concentration limit) so that a detached plasma state (characterized by cold plasma in the range 5-10eV) can build up [20].

### 1.3 Operation and maintenance

While the targets are subjected to particle bombardment and HHF loads, the entire divertor is exposed to fast neutrons radiating from the plasma core. The intense neutron flux (~$10^{16}$-$10^{18}$/m²·s) generates strong volumetric nuclear heating via thermal moderation due to the elastic scattering by the coolant molecules and gamma ray emission due to nuclei excitation in the solid materials [21]. Fig. 3 shows the predicted distribution of nuclear heating power density plotted on the contour of the DEMO divertor cassette. In addition, X-rays due to Bremsstrahlung of electrons and the line emission of impurity atoms (near the separatrix X-point) produce radiation power [16, 20]. The heat is removed by active cooling.

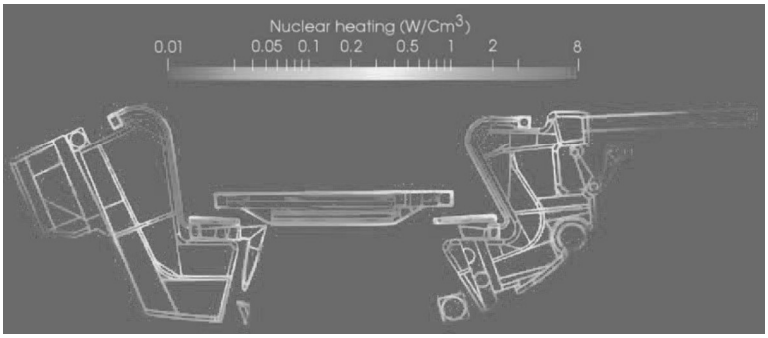


Fig. 3. Distribution of nuclear heating power density in the divertor cassette of the EU-DEMO.

Currently, the baseline design is based on pressurized-water cooling operated at a relatively lower temperature range compared to a PWR (~280-320°C). The baseline cooling scheme employs a separate dual cooling circuit system where each circuit is dedicated for either the targets or cassette body (CB). The cooling circuits are operated at separate temperature and pressure levels. The rationale and details of this decoupled cooling scheme is elucidated later (chapter 4). The coolant feeding pipes and the outlet pipes are routed through the allocated lower port and connected to the primary heat transfer system (PHTS) of the plant where the exhaust heat can be used for preheating the fresh coolant [11].

A certain number of the lower ports will be reserved exclusively for pumping. A pump system (e.g. diffusion pump combined with a metal foil pump or multi-stage cryopump) is stationed in the rear casks connected to the lower port within the confinement barrier (see Fig. 4, readers are referred to [22] for details). As the space of the plasma core acts as a perfect sink for the neutral gas, a strong pumping capacity as well as high gas conductance are required to maintain a sufficient gas throughput rate. In this context, the gas flow channels (gaps and duct) formed by the contour of the cassette configuration play a fundamental role in fostering gas exhaust and in hindering gas upstreaming and reflux [8]. The recommended pumping speed is 100-130m³/s for $D_2$ per port (pumped by the combination of metal foil pump and linear diffusion pump) and 4m³/s for He per port (pumped by the 2nd diffusion pump) [22].

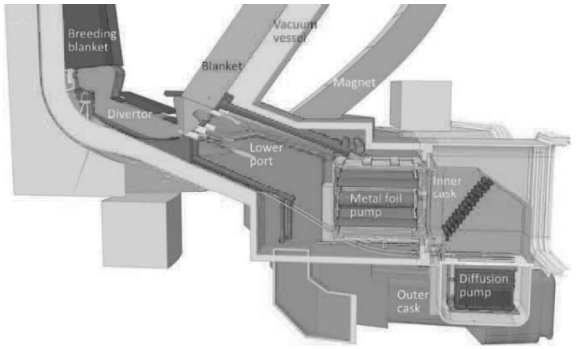


Fig. 4. Lower port region and the rear casks of the European DEMO design [23].

The plasma state in front of the divertor targets shall be monitored by in-situ diagnostic tools such as thermo-current measurement in order to detect a plasma reattachment event so that a detached state can be recovered by means of active controlling. To this end, full electrical insulation of the targets from the cassette body (except for a shunt) is necessary.

The sacrificial armor of the targets protects the water-cooled heat sink (pipes) from a direct contact with plasma. In normal and off-normal operation situations, the armor material is subjected to diverse surface erosion processes. The ratio of the front face armor thickness to the average erosion rate determines the erosion lifetime of the targets. Edge localized modes (ELMs) with the particle energy of a few keV will have a decisive impact on the erosion lifetime [8, 20, 24].

The lifetime of the structural materials (copper alloy, steel) is likely to be affected by neutron irradiation due to embrittlement and reduction of strength. The impact of irradiation on structural integrity depends on temperature and stress state during operation.

Once the end of design life has been reached (by erosion or irradiation), the divertor must be refurbished. The maintenance shall be performed by means of remote handling tools in a radioactive environment. The end effectors access the cassettes through the respective lower port. In case a cassette module needs to be replaced, the cassette is moved using the toroidal transport rail.

### 1.4 Alternative divertor configurations

Even though the current DEMO design is based on the single null divertor configuration as baseline, further selected alternative configurations are also under consideration for a possible down-selection at a later stage [25]. The decision of down-selection will depend on the outcomes of the extensive physics

as well as engineering studies (remote maintenance, magnets, costs, etc.). Fig. 5 shows four examples of the alternative configurations (as of 2018). Illustrated are the X divertor, super X divertor, snowflake divertor and double null divertor (f.l.t.r.) [12]. These configurations commonly feature a widely expanded plasma footprint aiming at a smeared heat flux peaking on the targets (for details, readers are referred to [26]).

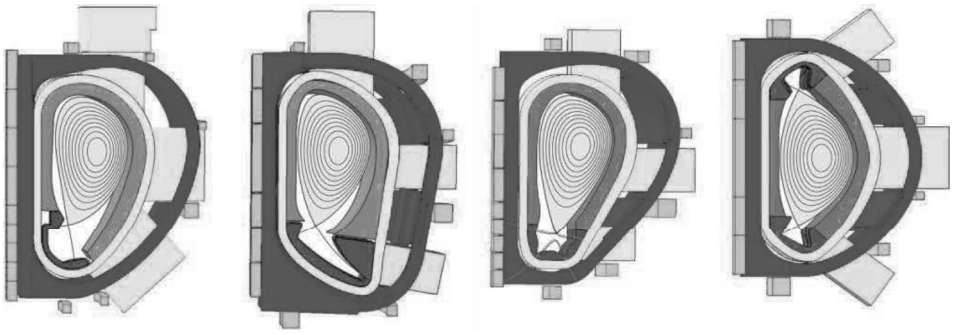

Fig. 5. Magnetic configurations of the alternative divertor concepts considered for the European DEMO (2018 version) [12]. (f.l.t.r.: X divertor, super X divertor, snowflake divertor, double null divertor). (Copyright 2019, Courtesy from IoP/IAEA)

### 1.5 Alternative target technology options

During the PCD phase, preliminary exploring studies were performed for a few alternative divertor target technologies other than the current baseline. The alternative technologies included liquid metal target (e.g. capillary porous armor system using a lithium bath) [27], helium-cooled target (tungsten monoblock design equipped with multi-jet injection dual pipes) [28] and water-cooled heat pipe target [29]. The R&D progress of these concepts is still at an early stage and thus they are regarded as long-term potential options (not necessarily to be pursued).

## 2. Loads and requirements

In this Section, the plant-level loads and the high-level system requirements imposed on the DEMO divertor are described. Design strategy and engineering approaches are subordinate to these.

### 2.1 Extrinsic loads

In Table 2, the extrinsic loads specified as design values for the currently assumed operation scenarios are listed [30]. These load values can be regarded as working hypotheses at the present stage (as of 2020).

Table 2. Extrinsic loads specified for the European DEMO divertor (as of 2020) [30].

| ID | Loads | Specifications |
|---|---|---|
| Load-1a | Volumetric thermal power<br>Volumetric thermal power density | ~139MW (by nuclear heating)<br>≤8MW/m³ |
| Load-1b | Baking temperature | ~240°C (uniform heating) |
| Load-2a | Surface thermal power on the targets<br>(Total radiation fraction: 90%) | ~45MW (by charged particles)<br>~108MW (by SOL radiation) |
| Load-2b | Peak heat flux density on the targets<br>in normal operation | ~10MW/m² (2h) |
| Load-2c | Peak heat flux density on the targets<br>in slow transients (thermal equilibrium) | ~20MW/m² (~10s) |
| Load-2d | Peak heat flux density on targets<br>in short transients (no thermal equilibrium) | ≤70MW/m² (~100ms)<br>with sweeping (e.g. 1Hz, 0.2m) |

| | | |
|---|---|---|
| Load-2e | Energy deposition on targets<br>upon fast transients (as off-normal events) | ≤150kJ/m² |
| Load-2f | Energy deposition upon central disruption | ≤1GJ (~10 ms) |
| Load-2g | Surface heat flux density due to neutral particles | ~2kW/m² (baffle region) |
| Load-3a | Surface thermal power due to core radiation | ≤78MW |
| Load-3b | Surface heat flux density due to core radiation | ~1MW/m² |
| Load-4 | Peak electromagnetic impact load<br>(downward disruption) | ~1.3MN (vertical)<br>excl. dynamic amplification (tbd.) |
| Load-5 | Particle flux density along the SOL | $\sim 10^{24}$/m²·s (≤10eV) |
| Load-6 | Neutron flux density in the surface layer | $\sim 1.7\times 10^{18}$·n/m²·s |
| Load-7 | Coolant pressure at the circuit inlet | ~5MPa (targets)<br>~3.5MPa (cassette body) |
| Load-8 | Coolant water chemistry (radiolysis) | t.b.d. |

## 2.2 Design requirements

In Table 3, the high-level system requirements are described with the underlying rationales.

Table 3. High-level system requirements imposed on the European DEMO divertor.

| ID | Descriptions |
|---|---|
| SR-1 | The divertor shall reliably perform the key functions over the entire lifetime withstanding the extrinsic loads and the induced effects of the loads (e.g. secondary stresses, armour surface erosion, material damage, corrosion, etc.). |
| SR-2 | The specified minimum lifetime (interval between replacements) is 1.5fpy[1)].<br>*Rationale*:<br>Operational lifetime is specified considering a reasonable balance between the power plant availability and structural/functional reliability. This requirement is of tentative nature since materials data from relevant irradiation tests are very limited. The initial lifetime shall be redefined again once materials data and design criteria from dedicated irradiation tests are available, also taking into account the evolving maintenance scheme. |
| SR-3 | Tungsten shall be used as plasma-facing armour of PFCs.<br>EUROFER97 steel shall be used as structural material for the cassette body and fixation units.<br>*Rationale*:<br>The material options should comply with the high-level requirements such as physical compatibility with fusion plasma (for PFCs) and reduced activation to assure recyclability (for major structures). |
| SR-4 | The design concept should be able to be realized by means of feasible technology options (≥TRL[2)] 4 at the 3rd Gate review in 2027) within an acceptable cost frame and the DEMO project timeline (EDA[3)] phase from 2028 on).<br>Technology maturity shall be evaluated at the 2nd Gate review in terms of the technology readiness level (TRL). |
| SR-5 | The divertor (incl. pipework) shall be compatible with the interfacing plant sub-systems. |
| SR-6 | The divertor must protect adjacent Vacuum Vessel (VV) (AISI 316LN-IG) and magnets from neutron radiation keeping nuclear loads below the specified limits.<br>- max. allowable irradiation damage dose limit in VV: 2.75dpa[4)]/6fpy [31]<br>- max. allowable nuclear heating limit in superconducting magnets: 50W/m³ |

[1)] fpy: full-power-year (of operation), [2)] TRL: Technology Readiness Level, [3)] EDA: Engineering Design Activity, [4)] displacement per atom

## 3. Baseline design concept

In this Section, the baseline design (as of 2020) of the DEMO divertor is briefly described. In mid-2020, the final version was validated by the Design Review Panel.

### 3.1 Design approach and constraints

Functional performance (cooling, shielding, pumping), structural integrity and longevity are three key design aspects. Issues related to (industrial) manufacturability, costs, waste hazard and safety are further design concerns. The envisaged lifetime (specified for the baseline design) is 1.5 full power year (fpy). The refurbishment should take place ex-situ in a hot cell outside the tokamak building. It was assumed that the DEMO divertor would not need to be classified as a SIC (Safety Importance Classification) component because the divertor was not supposed to have the containment function [32]. As a non-SIC component, divertor design can be exempted from those licensing regulations that are mandatory for a nuclear pressure equipment (e.g. ESPN order). It is accepted to produce a limited amount of low/medium level wastes which have an acceptable decay time (reaching the hands-on level after a few centuries). Based on these considerations, the following approaches were adopted:

1) Pursue maximum possible HHF technology limit to achieve a sufficient operational margin.
2) Where reasonably applicable, use mature (and commercially available) materials or technologies.
3) Where required, develop and apply advanced materials or technologies.
4) Take evolutionary R&D paths to exploit the state-of-the-art ITER technology.
5) Assure the design and technology against all expected operational anomalies.
6) Apply both design-by-analysis and design-by-experiment (still non-nuclear) approaches.
7) Find a pragmatic compromise between competing requirements (e.g. critical heat flux margin vs. low-temperature embrittlement)

### 3.2 Overall architecture

Fig. 6 shows the global CAD configuration model of the entire divertor (seen from three viewing angles). The divertor consists of 48 cassette modules arrayed symmetrically along the toroidal orientation. The divertor is divided into 16 sectors. Each sector comprises equally a set of 3 modules (1 central cassette and 2 side cassettes). Each sector is associated with a lower port through which the feeding pipework is routed. The toroidal angular range of a sector is 22.5°.

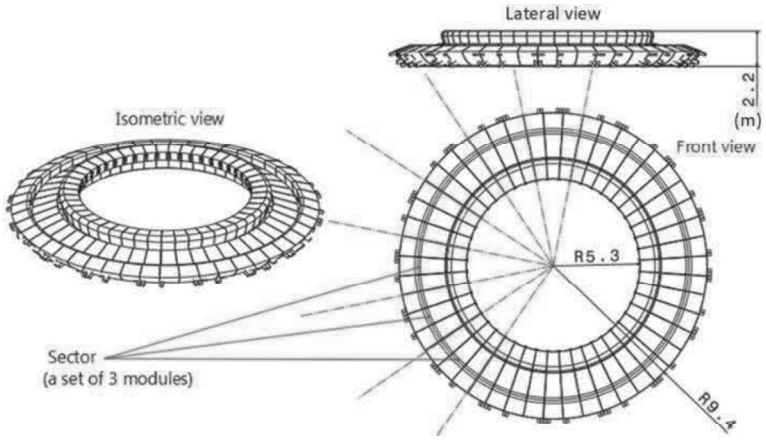


Fig. 6. Global CAD configuration model of the entire DEMO divertor (seen from 3 viewing angles)

Fig. 7 shows the CAD configuration model of a typical sector consisting of three cassette modules (left: top view, right: view through the lower port). The cassettes in the sector are almost identical except for some minor differences. The spacing between two adjacent cassettes is 20mm.

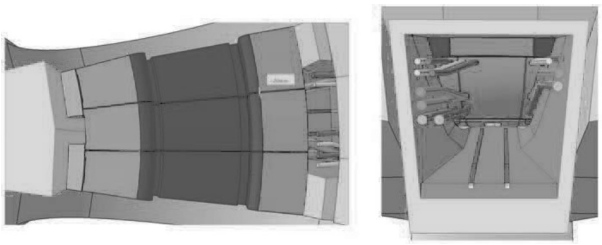

Fig. 7. A typical sector consisting of three cassette modules (left: top view, right: view through the port).

The CAD model of a typical divertor cassette module is illustrated in Fig. 8. A cassette module occupies the toroidal angular range of 7.5°. In Table 4, the major design constituents are listed with a brief description of the functions.

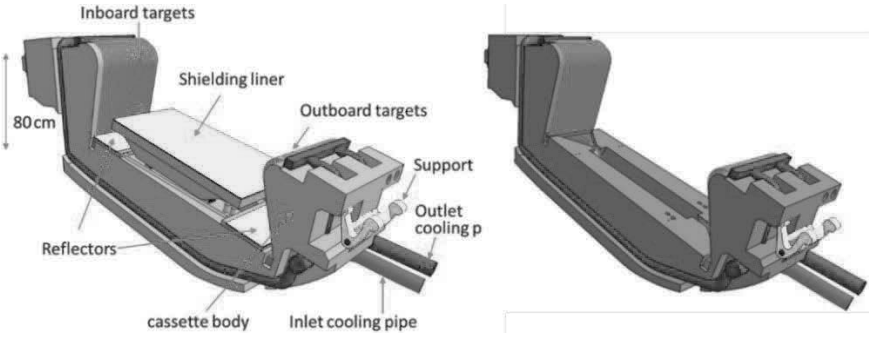


Fig. 8. A typical divertor cassette module (left: fully equipped, right: bare cassette body)

Table 4. Major constituents of a divertor cassette module and the functions

| Subcomponents /empty weight (kg) | Functions |
|---|---|
| Cassette Body (CB)<br>/5650<br>/6918 (with coolant) | • holds all sub-components.<br>• protects the VV from neutron flux and radiation.<br>• provides flow channels to exhaust gas.<br>• exhausts heat from nuclear heating. |
| Inner Vertical Target (IVT)<br>/345 | • intersects and neutralizes the SOL particle flux (inboard).<br>• exhausts heat from SOL particles, radiation and nuclear heating. |
| Outer vertical target (OVT)<br>/471 | • intersects and neutralizes the SOL particle flux (outboard).<br>• exhausts heat from SOL particles, radiation and nuclear heating. |
| Shielding Liner (SL)<br>/1186 | • shields the CB pumping duct to protect the VV from neutron flux and X-point radiation.<br>• provides gas flow channels pressing the exhaust gas.<br>• prevents upstreaming and reflux of gas into the plasma.<br>• exhausts heat from nuclear heating and X-point radiation. |
| Reflector Plates (RP)<br>/64, 91<br>/31 (supports) | • protect the cooling manifolds from neutron, particles and radiation.<br>• exhaust heat from nuclear heating and radiation. |
| Cooling pipes & manifolds<br>/281 | • transport coolant for feeding and circulation. |
| Cassette fixation supports (inboard/outboard CFS)<br>/132 (wishbone) | • attach and fix the CB to the VV (inboard, outboard).<br>• provide elastic compliance for preloading and for compensating the mismatch of differential thermal strains between CB and VV. |

| | |
|---|---|
| Central Cassette Outer Rail (CCOR)/2704 (total) | • provides a supporting interface between the central CB and the VV for toroidal transport of a module. |
| Inboard Toroidal Transportation Rail (ITTR) | • support CB against the gravity load during toroidal transportation.<br>• accommodate in-vessel magnet coils for strike point sweeping. |

For realizing system integration, numerous interface issues must be considered on the plant level:

- Compatibility of the CFS, CB and CCOR design with the remote handling scheme
- Compatibility of the feeding and outlet pipes with the lower port configuration
- Interface between the CB and the inboard in-vessel coils and toroidal transport rail
- Gas conductance for pumping
- Nuclear shielding for the VV and the magnets
- Connection of the cooling circuits to the PHTS, etc.

### 3.3 Cassette body [14, 15, 33, 34]

The CB accommodates and holds all subcomponents of a cassette module (see Fig. 8). A square-shaped pumping duct is located in the central region penetrating through the CB. This duct is the main gas flow channel towards the pumping ports. The CB hosts many internal chambers separated by ribs. The CAD drawings in Fig. 9 show the typical interior cut views of the CB (together with the SL and RPs). The ribs are 20mm thick, the outer wall is 30 mm thick. The ribs act as stiffeners for structural robustness and as partition walls (with holes) at the same time for guiding coolant streaming. The structural material of the CB is EUROFER97 steel [35]. One of the side walls has a trench to shield the cooling pipe.

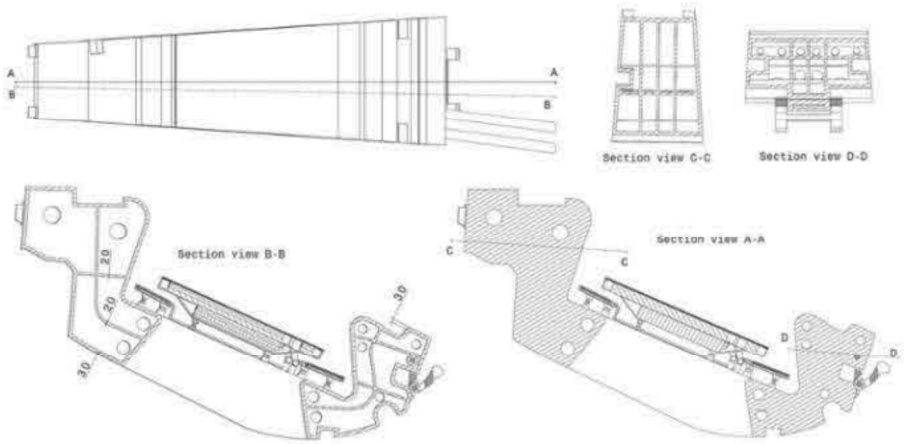


Fig. 9. Technical drawings showing the cut views of a cassette body with shielding liner and reflectors.

### 3.4 Targets (inboard/outboard) [14, 15, 34, 36, 37]

Each cassette module is equipped with a pair of IVT and OVT. The targets are deemed to be the most important and technologically critical component. The so-called ITER-like target design was chosen as baseline [38]. This design is characterized by tungsten monoblock armour and copper alloy cooling pipe. Fig. 10 shows the CAD model of the targets (a: IVT, b: OVT, c: coolant stream distributor manifold). The support legs are omitted in the figure for brevity. The planar area has the poloidal length of 700mm. The strike point is assumed to be located at the central region of the targets with a Gaussian distribution of power density (poloidal extension: ~100mm). The strike point will be swept over a poloidal range of ±200mm in an off-normal plasma reattachment event to mitigate the time-averaged heat flux. Each target plate consists of a parallel array of many target elements (IVT: 32, OVT: 44) in the toroidal orientation. The weight of the targets amounts to 345kg (IVT) and 471kg (OVT), respectively. The cooling pipes of each target are connected to the respective feeding pipe via a stream distributor manifold where 5 ribs act as baffle walls.

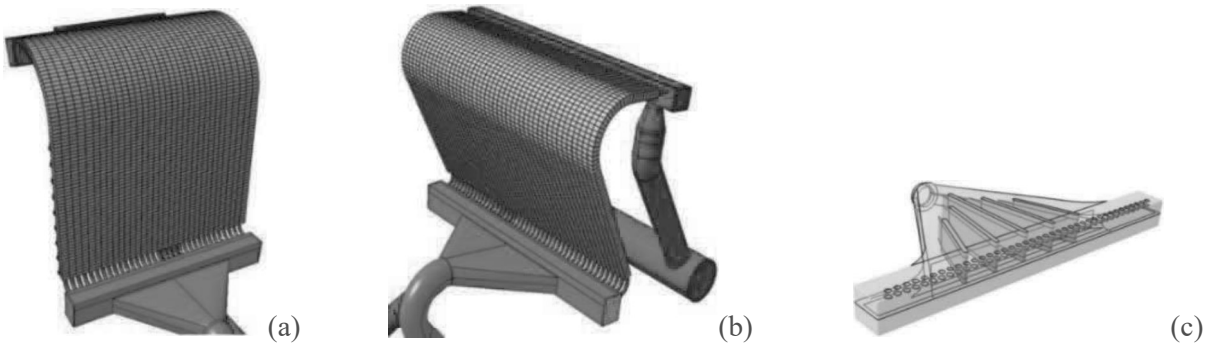

(a) (b) (c)

Fig. 10. Inboard (a) and outboard target (b) and coolant stream distributor manifold (c).

Each target element consists of a longitudinal array of rectangular tungsten armour blocks connected by a long cooling pipe (CuCrZr alloy) running through the center bore of the blocks. The pipe is joined to the blocks via a 1mm thick interlayer (soft copper). Fig. 11 shows the CAD model of a typical target element segment.

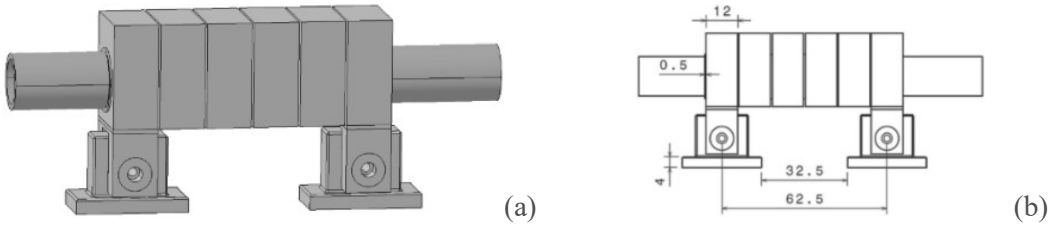


(a) (b)

Fig. 11. A typical target element segment (a) and the technical drawing (b).

Fig. 12 shows the CAD model of a typical single monoblock unit (a) and the technical drawing of the target cross section (b). The design is de facto identical to the ITER monoblock target design except for the section width (23mm instead of 28mm) [38]. The reduced width dimension has a beneficial effect with regard to structural integrity when a fatigue crack is initiated at the armour front face. In this case, the crack tip stress intensity is substantially decreased [39-41].

The rather thick front side armour thickness (8mm) was adopted to maximize erosion lifetime accepting higher surface temperature as trade-off. If the lifetime of the armour is not dictated by erosion, the initial armour thickness can be further reduced in favor of surface temperature. At 20MW/m², the front face temperature raises from 1300°C to 2400°C when the armour thickness increases from 4 mm to 10 mm [39]. Should the targets be subjected to slow transient events (~20MW/m²) several hundred times, the cumulative heat exposure time will be long enough to induce substantial recrystallization in the tungsten armour resulting in a considerable reduction of yield stress, particularly in the front face layer. This thermal softening promotes plastic fatigue potentially leading to a crack initiation [39]. However, the mock-ups of this baseline design showed no crack formation at all even after 1000 loading cycles at 20MW/m² even though the upper half of the armour had been fully recrystallized. This issue will be revisited later (chapter 7). Under the normal operation condition (~10MW/m²), the temperature at the front face of the 10mm thick armour is not higher than 1300°C. Thus, recrystallization of tungsten will not be an issue for the normal operation case.

The dimension of the interlayer and the cooling pipe were inherited from the ITER target design. The effect of the interlayer thickness with respect to structural integrity was studied in terms of fracture mechanics and HHF fatigue resistance (thickness range: 0.1-1mm) [42, 43]. These studies manifested a beneficial stress relaxation effect of the soft interlayer leading to a superior performance.

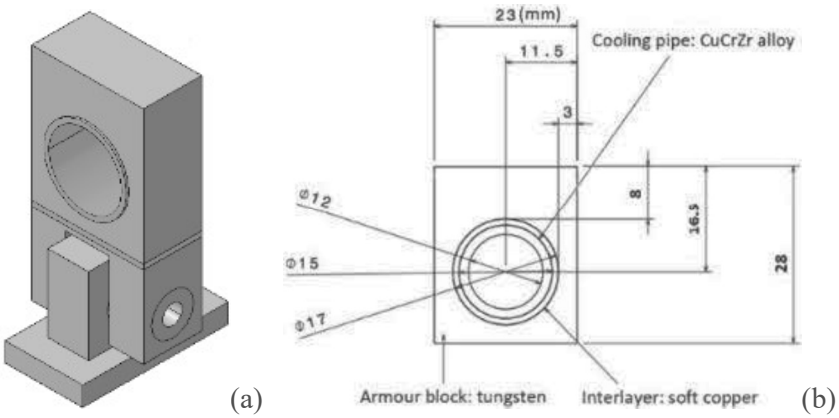

(a) (b)

Fig. 12. A typical single monoblock unit (a) and the technical drawing (b).

The design of the attachment legs was inherited from the ITER target design. The attachment unit is made of EUROFER97 steel. The steel legs are brazed to the tungsten blocks. The legs are fixed to the underlying plug by a pin and two pin locks at both ends. To ensure electric insulation of the target from the CB (except for one shunt position), the contact surfaces of all constituents within the attachment unit shall be coated with a thin ceramic film [37]. The insulation is required for a diagnostic purpose to detect reattachment events by measuring an abrupt change of thermo-currents. The axial gap spacing between two neighboring armour blocks is 0.5mm (possibly shall be reduced to 0.4mm). The materials specified for the target elements are listed in Table. 5.

Table 5. Materials specified for the target elements

| | |
|---|---|
| Armour block | Pure tungsten (hot rolled and stress-relieved) |
| Interlayer | Soft OFHC copper (casted) |
| Cooling pipe | CuCrZr alloy (seamless drawn) |
| Attachment unit | EUROFER97 steel |
| Insulation coating | Ceramic coating (oxides, nitrides) |

### 3.5 Shielding liner [14, 15, 33, 34]

Fig. 13 shows the CAD model of the SL. The technical drawing of the internal cooling channel architecture on the middle cross section is given in Fig. 14. The heat sink hosts three stack layers of cooling channels for effective cooling and moderation. The structural material is EUROFER97 steel. The front face must be armoured with a tungsten coating to ensure physical compatibility with the plasma and to protect the steel structure from neutrons and gas particles. The four multi-link supporting legs allow for differential thermal expansion of the SL relative to the CB. Each leg consists of two single hinges on the outboard side and two double hinges on the inboard side. The size of the legs was minimized to avoid overheating by nuclear heating. The dimensioning of the SL was made considering four factors:

- Cooling capacity to cope with the nuclear heating and radiation power (from the separatrix X-point)
- Structural resilience against impact loads and thermal stresses
- Nuclear shielding capacity for protecting the underlying supporting legs
- Gas conductance for particle exhaust

The cooling channel architecture is the outcome of an iterative thermo-hydraulic design optimization. The relatively complex geometry poses a technological challenge for manufacturing. There are still two critical design concerns:

- Excessive irradiation damage of the heat sink leading to embrittlement (remaining unsolved)
- Intensive nuclear heating of the supporting legs leading to thermal softening (within the limit)

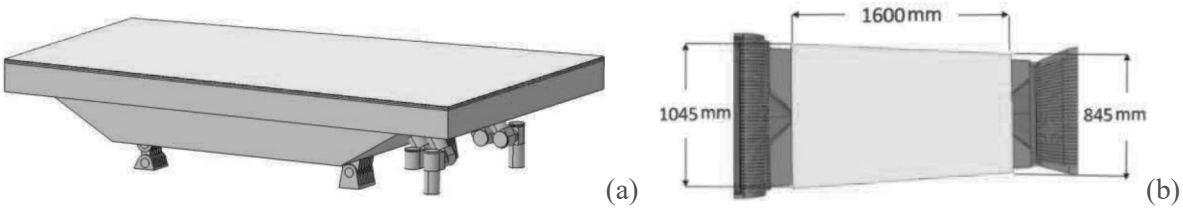

(a) (b)

Fig. 13. Shielding liner (a: whole structure, b: front face view, yellow plate only).

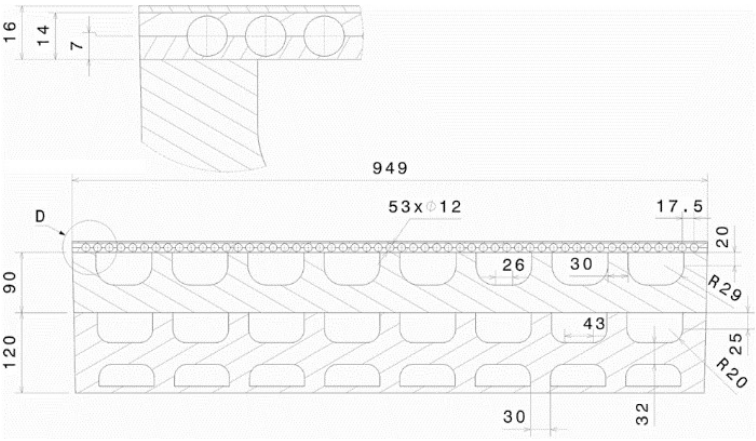


Fig. 14. Technical drawing of the cooling channel architecture in the shielding liner (middle section).

### 3.6 Reflector plates [34]

Fig. 15 shows the CAD model of the RPs (a: whole structure, b: inboard side). The RPs cover the feeding pipes of the targets and manifolds. The structural material is EUROFER97 steel. The front face is armored with tungsten coating (currently, 3mm).

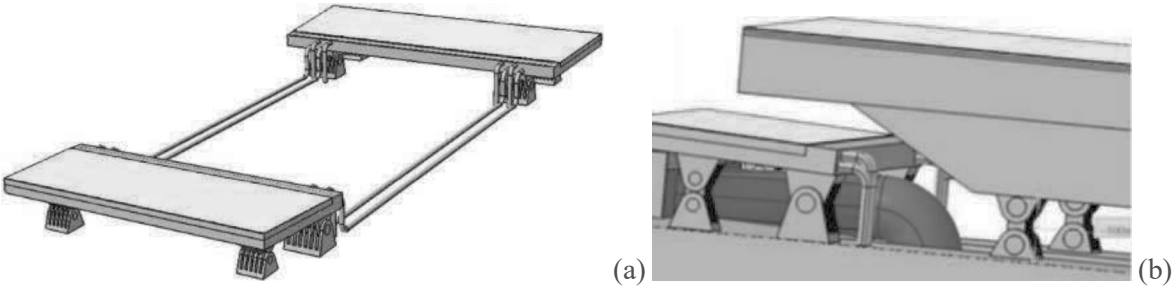
(a) (b)

Fig. 15. Reflector plates (a: whole structure, b: configuration of the inboard side).

Fig. 16 is the technical drawing of the cross section showing the internal cooling channel architecture. The cooling circuits of the inboard and outboard RPs are connected in series (heat flux: <1MW/m²).

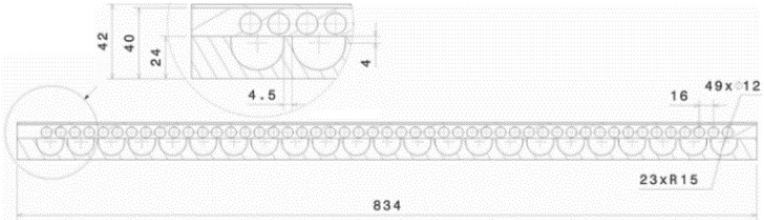


Fig. 16. Technical drawing of the reflector plate showing the cross section with the cooling channels.

### 3.7 Cassette Fixation Supports [15, 34, 44]

The CB is attached and fixed to the VV by means of the inboard and outboard cassette fixation support (CFS). In addition, the inward-oriented magnetic force exerting on the fully magnetized (ferromagnetic)

CB strongly (≤800kN) pulls the CB towards the inboard VV during operation [44]. This inward Maxwell force ensures electrical contact between the CB and the VV, but the strength of the force could decrease when the CB is irradiated if a reduced magnetization results [45].

Fig. 17 shows the CAD model of the inboard CFS. This CFS consists of a nose-socket pair featured on the inboard edge face of the CB and on the inboard wall of the VV, respectively. Once engaged, the locking gives rise to full constraints against toroidal and poloidal displacement maintaining the specified gap between the blanket edge and the CB.

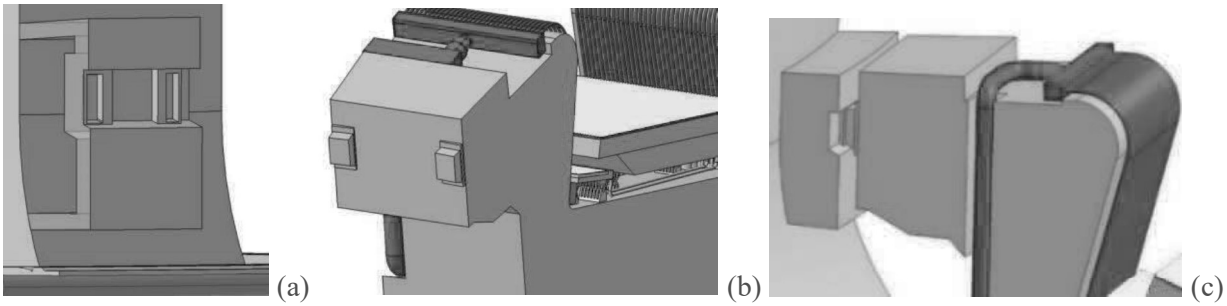

(a) (b) (c)

Fig. 17. Inboard cassette fixation support (a: socket, b: nose, c: view after locking).

Fig. 18 shows the CAD model of the inboard toroidal transportation rail (ITTR). During transportation, the cassette moves being supported by the roller bearings. The rail serves for two-fold functions:

- to offer static support against the gravity load of a cassette during toroidal transportation,
- to accommodate the in-vessel magnet coils (shielded by the CB) for strike point sweeping.

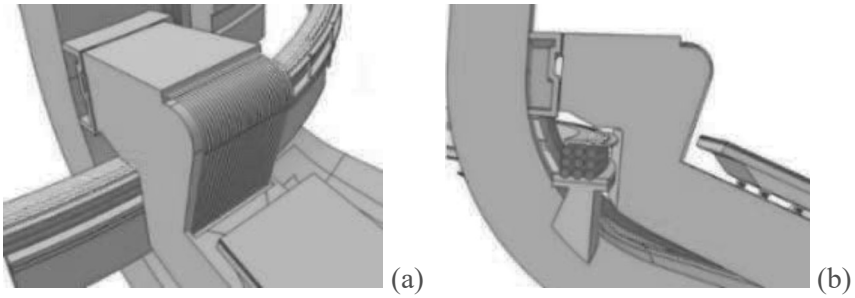

(a) (b)

Fig. 18. Inboard toroidal transportation rail supporting a cassette during toroidal transportation (a, b).

Fig. 19 illustrates the outboard CFS. The key element is the wishbone. In addition to the fixation function, the wishbone provides elastic compliance and static resilience to accommodate the mismatch in thermal strains between the CB and the VV. Noting that the temperatures assumed are still subjected to change during the design phase, the origins of this strain mismatch are:

- different coolant temperature during operation (CB: 180-210°C, VV: 40°C)
- different baking temperature (CB: 240°C, VV: 180°C)
- differential thermal expansion coefficients (CB: EUROFER97, VV: AISI 316L(N)-IG)
- different nuclear heating power density

The relative difference in the radial displacement due to differential thermal strains between the CB and the VV amounts to 5.6mm (compressive) during the normal operation and 1.5mm (tensile) during the baking. The wishbone must have a sufficient strength under such displacement loads. Ti-6Al-4V alloy was selected as material for the wishbone to exploit its high elasticity and strength. By means of a multi-step locking operation, the wishbone and the CB are put into elastic compression towards the inboard VV so that the CB is fixed, electrical contact is established and loads are transferred from the CB to the VV in the vertical and toroidal directions.

The elastic stiffness of the wishbone (Fig. 19 a) amounts to 30MN/m (<9 % of the CB). Degradation of elasticity by neutron irradiation was taken into account (decrease by 40% after 1.5 fpy). The pins (alloy 660 steel) have the diameter of 60-100mm to withstand the shear force (~800kN) under impact loads. A sufficient clearance is needed for the locking and unlocking operation.

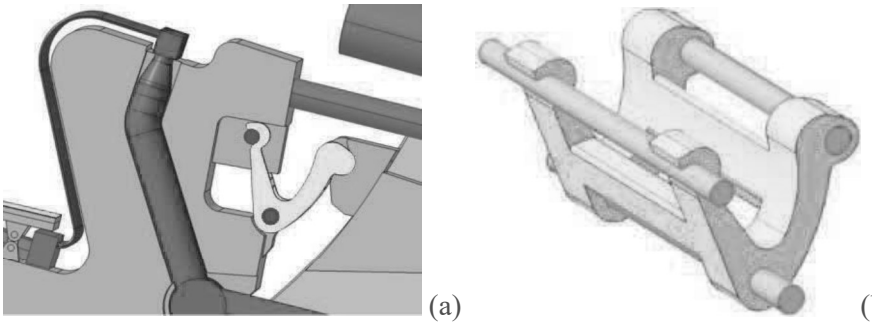

(a) (b)

Fig. 19. Outboard cassette fixation system (wishbone in yellow) (a), another wishbone variant (b).

## 4. Divertor cooling scheme

### 4.1 Requirements and constraints

The thermal loads listed in Table 1 indicate a drastic difference in the power density between the targets ($\leq$20MW/m$^2$) and the rest parts of the cassette ($\leq$1MW/m$^2$, $\leq$8W/cm$^3$). On the other hand, the acceptable service temperature ranges of the respective structural materials (IVT/OVT: CuCrZr-IG, CB/SL: EUROFER97) do not fully overlap with each other. These distinct differences implicate the necessity of a separate cooling scheme with two cooling circuits each dedicated for the HHF components (targets) or medium heat flux components (CB, SL, RP). The paramount cooling requirement for the HHF components is to ensure a sufficient margin to the critical heat flux (CHF) at the strike point under all off-normal operation events so that local film boiling is avoided (initial nucleate boiling is accepted). A similar requirement applies to the other components as well, but the criticality of the off-normal events is far less relevant.

From the cooling point of view, the coolant temperature should be kept as low as possible to maximize the margin to the CHF. However, from the structural reliability point of view, it is desirable to operate the (irradiated) components above the ductile-to-brittle transition temperature (DBTT) of EUROFER97 and the thermal recovery temperature of CuCrZr to maintain ductility. Unfortunately, the two contradictory requirements can hardly be satisfied simultaneously even if a dual cooling scheme with separate cooling circuits is adopted. Therefore, a prudent engineering compromise is inevitable.

### 4.2 Heat flux distribution

The distribution of the nuclear heating power density generated in the cassette is plotted in Fig. 20. The highly non-uniform power density is attributed to the rapid attenuation of neutron flux through the depth. The solid body exhibits a similar heat flux distribution as the coolant. Fig. 20 reveals that the heat flux density near the plasma-facing front face (5-8MW/m$^3$) is at least an order of magnitude higher than that of the rear parts (0.1-1MW/m$^3$) suggesting that the colder inlet coolant should be fed first into the front side (IVT/OVT and SL). The total volumetric thermal power (339MW) amounts to 17% of the fusion power. The individual contributions are broken down as follows (for the entire divertor) [44, 46, 47]:

- Volumetric heat in the solid body of the cassettes: 85MW
- Volumetric heat in the solid body of the supports: 17MW
- Volumetric heat in the coolant fluid of the cassette: 37MW
- Surface heat on the targets (by particles and radiation): 122MW
- Surface heat on the SL and RPs (by radiation): 78MW

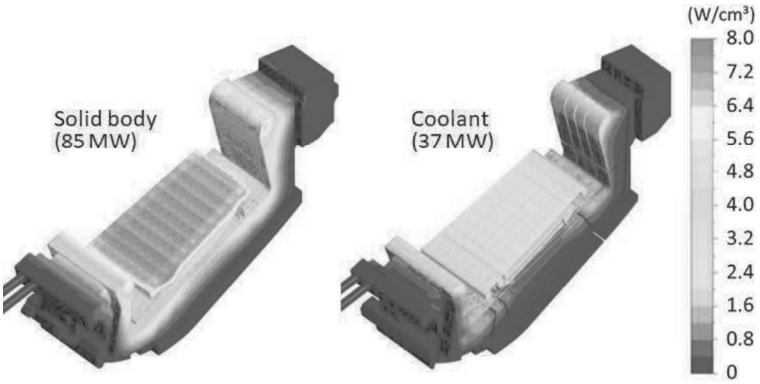


Fig. 20. Distribution of volumetric thermal power density generated by nuclear heating in the cassette (left: heat flux density in the solid body, right: heat flux density in the coolant fluid).

### 4.3 Cooling circuits and cooling conditions

In the PCD phase, the dual cooling scheme was adopted as baseline. The two cooling circuits are shown in Fig. 21 (a: cooling circuit of the CB, SL and RPs, b: cooling circuit of the targets). The cooling circuit of the targets comprises the pipework of the IVT and OVT connected in parallel by a feeding and exhaust pipe (DN125 schedule 40) via the distributor manifolds. The other cooling circuit consists of the cooling channels of the CB, SL and RPs. The latter circuit is the combination of a series connection (CB-to-SL, CB-to-RPs) and a parallel connection (SL-to-RPs) of the channels with a common feeding and exhaust pipe (DN80 schedule 40). The configuration and dimension is the outcome of an iterative hydraulics design optimization [48-53].

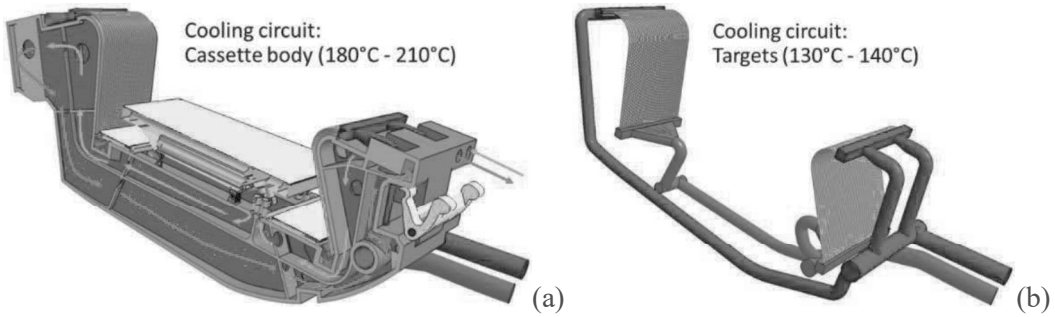


Fig. 21. Two cooling circuits of the baseline dual cooling scheme (a: cassette body, b: targets).

The hydraulic parameters of the coolant defined for the targets and the CB (incl. SL and RPs) are listed in Table 6 and 7, respectively [47, 54].

Table 6. Hydraulic parameters of the coolant defined for the targets.

| | |
|---|---|
| Mass flow rate per cassette | 99kg/s |
| Coolant temperature (inlet) | 130°C |
| Coolant pressure (inlet) | 5MPa |
| Temperature rise (outlet) | +6°C |
| Margin to the critical heat flux | >40% |
| Pressure drop (outlet) | <1MPa |
| Velocity (OVT) | 13-15m/s |

Table 7. Hydraulic parameters of the coolant defined for the cassette body, shielding liner and reflectors.

| | |
|---|---|
| Thermal power per cassette | 4.2MW |
| Mass flow rate per cassette | 31.2kg/s |
| Coolant pressure (inlet) | 3.5MPa |
| Pressure drop (outlet) | 0.6MPa |
| Coolant temperature (inlet) | 180°C |
| Temperature rise (outlet) | 30°C |
| Margin to the saturation temp. (outlet) | 22°C |
| Local max. temp. of coolant (bulk) | 230°C |
| Local max. temp. of solid (steel) | 555°C |
| Pumping power per cassette | 20kW |

The cooling conditions for the targets were derived from the requirement to ensure a safety factor of 1.4 (i.e. 40% margin) to the CHF (45MW/m² at the cooling pipe inner wall) under the applied front face heat flux of 20MW/m² (defined as technology goal) in thermal equilibrium (pulse: ≥10s) [55]. Assuming a swirled cooling pipe (inner diameter: 12 mm), the maximum possible local coolant temperature at the strike point is about 137°C (see Fig. 22), which is definitely lower than the thermal recovery temperature (150-200°C) of irradiated CuCrZr alloy [56, 57]. This conflicting circumstance is illustrated in Fig. 23.

The use of such a low-temperature coolant for the (irradiated) targets can be justified when a fracture mechanics-based structural design is applied. The toughness of irradiated (thus embrittled) CuCrZr alloy increases with decreasing temperature below 200°C [58]. The beneficial effect of this peculiar property was manifested in a theoretical study of the fracture behavior of a crack in the cooling pipe [59].

Furthermore, the inherent conservativism of the elastic design rules can be substantially relaxed if total ultimate tensile strain (≤6%) is adopted as failure criterion instead of uniform elongation limit (≤1%) for irradiated CuCrZr alloy [60, 61].

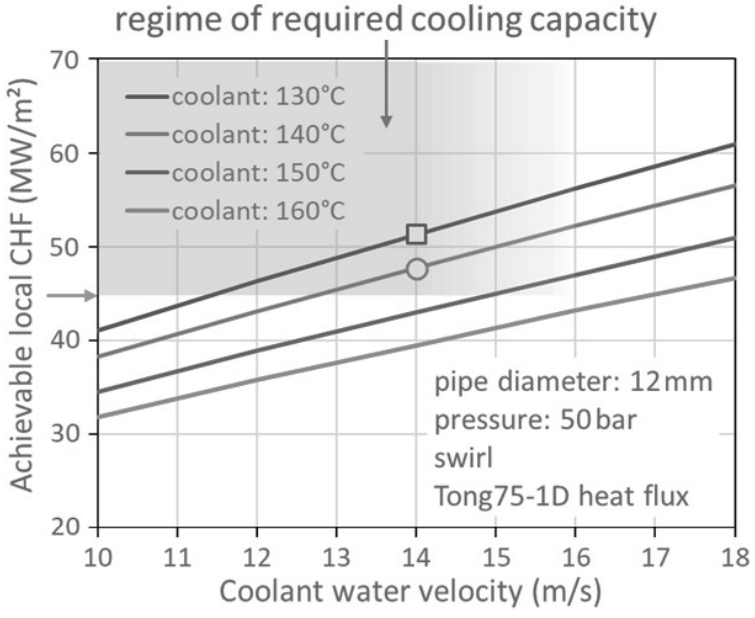


Fig. 22. Relationship between the local heat removal capacity at the inner wall of the (swirled) cooling pipe (inner diameter: 12mm), coolant velocity and the coolant bulk temperature. [55].

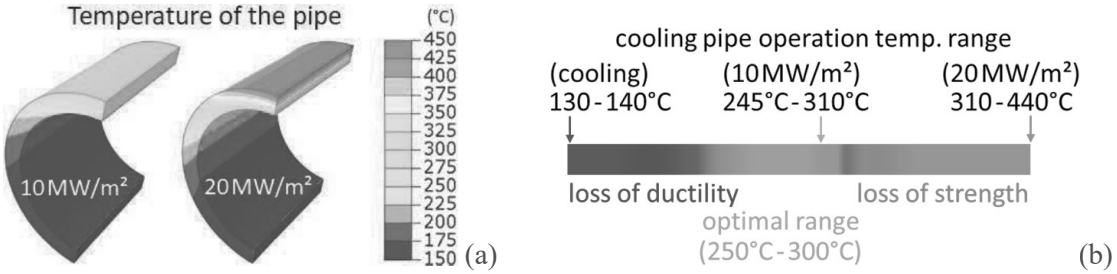


Fig. 23. Equilibrium temperature distribution in the cooling pipe of the target under two representative thermal load cases at the strike point (a), predicted operation temperature range of the cooling pipe under HHF loads up to 20MW/m² (b) [59].

The coolant of the CB was set to a temperature range from 180°C (inlet) to 210°C (outlet), which lies far below the desired temperature range (300-550°C) of irradiated EUROFER97 steel. The reason for taking this low-temperature coolant is the same as the case of the targets, namely, to prevent bulk boiling crisis as well as sub-cooled film boiling. On the other hand, the local temperature in the highly stressed regions should be higher than the fracture toughness transition temperature (FTTT) of irradiated EUROFER97 steel (see Section 5.1). This rationale tacitly assumes that a fracture mechanics-based non-ductile design rule shall be applied. The detailed description of this issue is found elsewhere [62, 63].

### 4.4 Cooling performance [47, 54]

The cooling scheme was verified by computational fluid dynamics analyses to demonstrate a reasonable cooling performance. The overall thermohydraulic coolant behavior of the both circuits are presented in Fig. 24-29. Fig. 24 depicts the coolant stream lines and the axial velocity field in the OVT. A highly uniform velocity distribution across the pipes is seen (average: 14.4m/s, deviation: 0.3m/s).

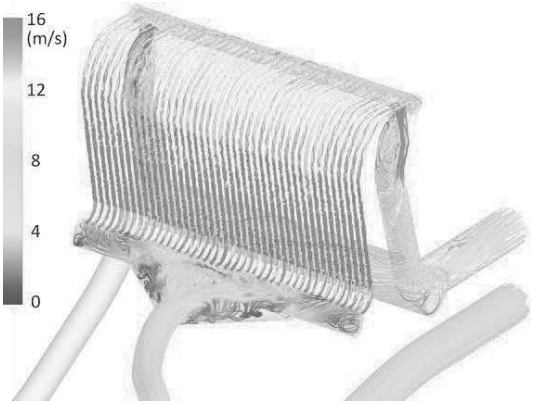


Fig. 24. Coolant stream lines and axial velocity field in the OVT.

Fig. 25 shows the coolant pressure field in the target cooling circuit. The total cumulative pressure drop is less than 1MPa, which is fully acceptable. The pressure drop is caused mostly (84-93%) due to the turbulence loss in the diffuser manifolds and the friction by the swirl tapes The average margin to the CHF at the strike point reaches 43% (inboard) and 52% (outboard). Thanks to the hydraulic uniformity in the toroidal direction, all target elements exhibit a similar heat removal capacity (deviation: 1-2%).

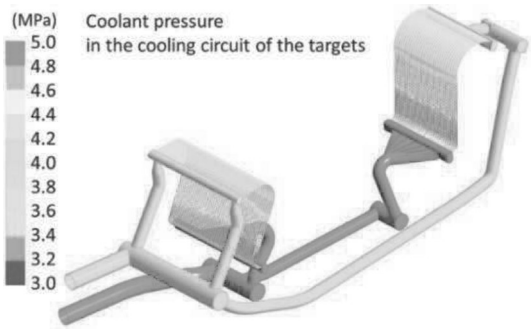


Fig. 25 Pressure field of the coolant in the target cooling circuit.

Fig. 26 shows the pressure and the temperature field of the coolant in the CB, SL and the RPs. The total cumulative pressure drop (except for the targets) amounts to 0.6MPa, which is fully acceptable. 64% of this pressure drop occurs in the SL whereas the CB gives a contribution of only 25%. The coolant temperature exhibits a uniform distribution except for the cold outboard inlet region. The total temperature rise amounts to 30°C. The margin against the saturation temperature at the CB outlet amount to 22°C. The SL and the RPs exhibit a huge margin to the respective CHF (SL: 630%, RPs: ≥150%).

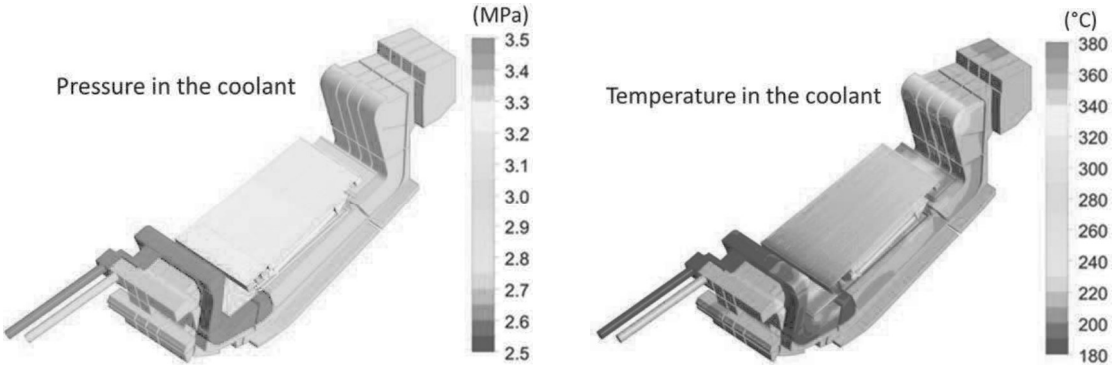


Fig. 26. Pressure and temperature field of the coolant in the cassette body, shielding liner and the reflector plates.

Owing to the limited pressure drop (decrease by 17% in total) in the cassette, the decrease of the coolant saturation temperature is accordingly small (<10°C). The margin between the local coolant temperature and the critical temperature of coolant vaporization (saturation temperature) is mostly larger than 10°C as revealed in Fig. 27 (a). However, there is a region of concern near the front face of the upper inboard wing where this margin diminishes or even is exhausted (indicated in grey). In this region, the absence of fast flows close to the wall is responsible for the impeded heat transfer (see Fig. 27 (b)). The layer of this critical region is tenuous, thus a sub-cooled film boiling at the fluid-wall interface is more likely to occur rather than bulk vaporization. Here, a further optimization is needed (e.g. higher inlet pressure).

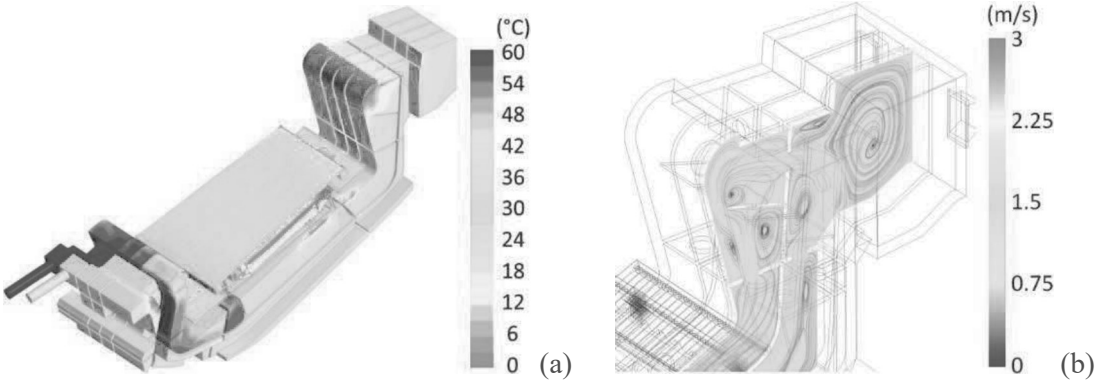

Fig. 27. (a) Margin between the local coolant temperature and the critical temperature of coolant vaporization, (b) 2D section view of the fluid flow field in the inboard wing of the cassette body. The regions of negative margin are indicated in grey.

Fig. 28 shows the equilibrium temperature distribution building up in the solid body (steel) of the cassette. The total temperature range spans from 200°C (the rear regions) to 555°C (the SL legs), but for the most part of the CB, the temperature is below 250°C. In this 'cold' region, the irradiation damage dose rate ranges from 0.1 to 2dpa/fpy. This means that the irradiated CB would remain mostly in a non-ductile state (if not fully embrittled) after a certain operation period.
For this embrittled region, the structural integrity must be verified based on proper failure criteria capturing fast fracture and fatigue crack growth [64]. In this practice, the dependence of toughness and fracture mode on multiple parameters (temperature, damage dose, stress tri-axiality and equivalent stress) must be considered. The lack of credible material data is a major issue.
The temperature hot spots (555°C) appear in the supporting legs of the RPs. The SL and the baffle apex experience high temperature (450-500°C) too. The maximum solid body temperature remains below the allowable upper limit temperature (~550°C) preserving the long-term mechanical stability (≥2000h) [65].

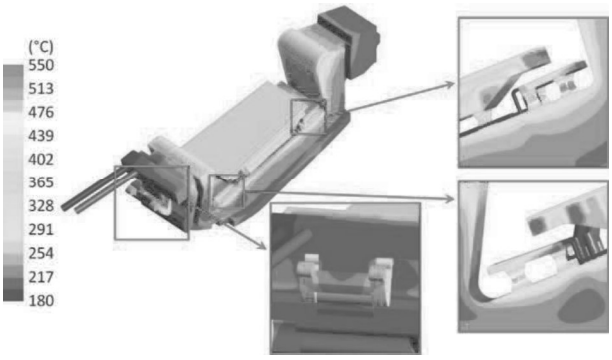

Fig. 28. Equilibrium temperature distribution building up in the solid body (steel) of the cassette.

## 5. Nuclear loads and shielding performance

### 5.1. Irradiation damage [46]

The use of low-temperature coolant (180-210°C) for the steel structures poses a strict constraint on the maximum permissible irradiation damage dose. Unfortunately, there is no test data of EUROFER97 steel irradiated at such low temperatures. Based on the toughness data of EUROFER97 irradiated at 300°C, the maximum allowable damage dose was identified to be 6dpa [63]. The rationale was that the inlet coolant temperature (thus the lowest solid temperature) should be higher than the measured FTTT (~175°C). As the DBTT of EUROFER97 does not appreciably change when irradiated at the temperature range of 250-350°C [62], this specification is deemed a pragmatic approach to start with even though the irradiation-test temperature does not exactly match the operation temperatures. Currently, a dedicated irradiation test at 150-200°C is under planning to ascertain the low-temperature irradiation effects.

Fig. 29 shows the distribution of irradiation damage from a neutronic analysis computed for the steel bodies of the cassette where the damage dose is plotted in the unit of dpa/fpy. The maximum damage (5dpa/fpy) occurs in the heat sink of the SL and the apex of the both baffles. This means that the SL will reach the 6dpa limit already after 1.2fpy, that is earlier than the targeted lifetime of 1.5fpy. The supporting legs of the targets experience high damage (4dpa/fpy) as well. Unfortunately, it seems very difficult to mitigate the irradiation damage in the plasma-facing front regions due to the direct exposure to the intensive neutron flux. A relaxed conservativism of a (fracture mechanics-based) design rule may be needed to justify the required lifetime.

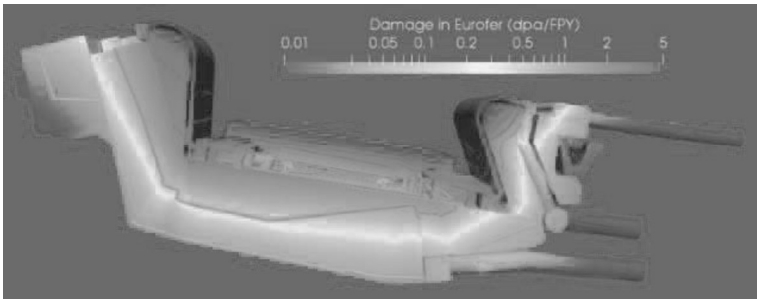

Fig. 29. Distribution of the irradiation damage in the steel components of the cassette (unit: dpa/fpy).

Fig. 30 shows the predicted distribution of the helium concentration produced by nuclear transmutation. Helium tends to cluster forming stable gaseous bubbles segregating at the grain boundaries at elevated temperatures. High helium concentration has a critical impact on the weldability of steels, a critical issue for the cutting/rewelding of the feeding/exhaust pipes during a remote maintenance. For the irradiated feeding/exhaust pipes (AISI 316 L(N)-IG or EUROFER97), the 1appm (atomic parts per million)-limit was specified. The rear part of these pipes behind the CB (denoted in blue in Fig. 30) meets this criterion. On the contrary, the red region where helium concentration reaches 100appm allows neither recycling nor cutting/rewelding. It is believed that the stable helium gas bubbles can be removed only by melting (annealing is not feasible).

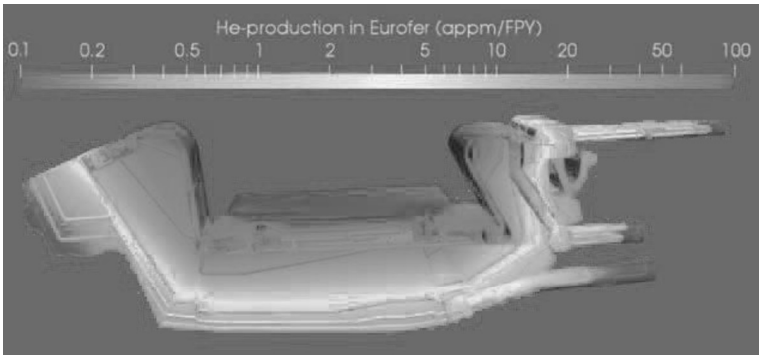

Fig. 30. Distribution of helium concentration produced by nuclear transmutation (unit: appm/fpy).

The nuclear loads in the targets are of critical importance for the lifetime as well. Fig. 31 shows the distribution of the damage dose in the tungsten amour of the IVT, OVT and the SL in the unit of dpa/fpy. The damage dose of the tungsten armour reaches the maximum at the upper baffle regions (1.9dpa/fpy) and decreases gradually towards the strike point (1dpa/fpy). The armour of the SL experiences the same damage dose (1dpa/fpy). The helium concentration in the tungsten amour is modest (1.4appm/fpy) [66].

The damage dose in the copper alloy cooling pipe reaches up to 7dpa/fpy (end-of-life dose: 10.5dpa) [67]. This damage regime is currently not covered by the ITER materials properties handbook. However, considering the pronounced mechanical saturation behavior of irradiated CuCrZr alloy already after a low irradiation dose (<1dpa), it was tentatively assumed that the key mechanical behavior of irradiated CuCrZr alloy would not significantly change at least up to 10dpa [57]. The helium production rate in the copper cooling pipe reaches up to 58appm/fpy, which is substantial. The high helium concentration will cause considerable embrittlement even at elevated temperatures (≥250°C) due to segregation of helium bubbles at the grain boundaries. The same issue applies to the copper interlayer [59, 68].

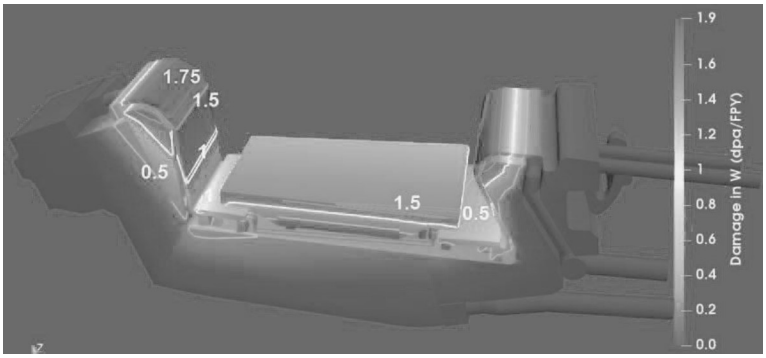

Fig. 31. Distribution of damage dose in the tungsten amour (unit: dpa/fpy).

5.2 Nuclear shielding performance [46]

As nuclear shielding for the VV is one of the key functions of the divertor, the shielding performance must be carefully assessed. For the VV (AISI 316L(N)-IG steel), the maximum allowable nuclear load was specified in terms of the "negligible irradiation damage dose limit" as defined in RCC-MRx (A3.3S.33) [69]. According to this criterion, the irradiation damage dose should not exceed 2.75dpa at the end of the service life (6fpy). The negligible damage dose limit is based on the premise that the loss of ductility or toughness due to irradiation should be less than 30%. This means that the fracture energy ($J_{Ic}$) decreases from 500kJ/m² to 350kJ/m² for the irradiation temperature range of 20-375°C at 2.75dpa.

Fig. 32 shows the distribution of the irradiation damage dose in the bottom region of the VV after 6fpy. The peaking hot spot is located directly below the CB pumping duct where the maximum value of the damage dose reaches 1dpa, which is significantly lower than the specified criterion. This damage dose can be further reduced if a few beam-like (water-cooled) shielding inserts are introduced in the pumping duct in order to block neutron streaming [33]. With these inserts the VV lifetime can be extended up to 30fpy (≤2.5dpa/30fpy). The nuclear shielding for the magnets is primarily dictated by the geometrical configuration of the lower ports and the port shielding strategy while the divertor design per se only has a limited impact. Currently, the peak nuclear heating power at the hot spots in the TF coils amounts to 150W/m³ (allowed limit: ≤50W/m³) [23].

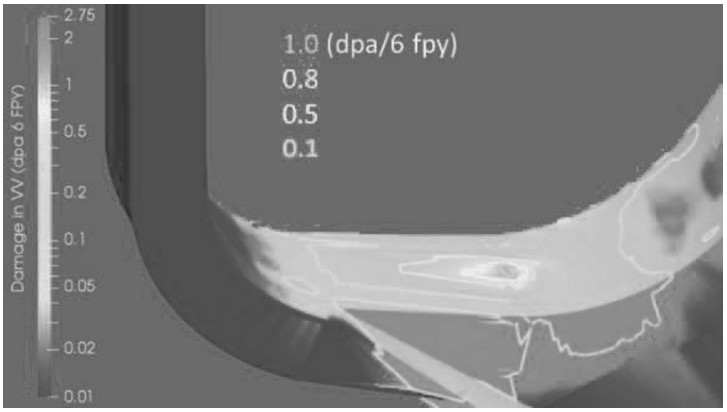

Fig. 32. Distribution of the irradiation damage dose in the bottom region of the VV after 6 fpy.

## 6. Structure-mechanical performance

6.1. Structural integrity assessment: challenges and approaches

The structure-mechanical performance of the divertor can be evaluated in terms of diverse failure criteria for various operational loading conditions. Comprehensive structural integrity assessment studies were carried out to support the design activities. In the absence of a DEMO Design equivalent of the ITER SDC-IC [70] (yet to be developed within the program), the structural design rules (elastic/elasto-plastic,

monotonic/cyclic) of RCC-MRx code (AFCEN ed.) were applied for the steel structures (CB, SL) [71-74].
For the targets, however, there is no well-established rule. The monoblock-type joints consisting of dissimilar materials each having a distinctively different yield stress poses a particular challenge for stress analysis. Moreover, combined loads, cyclic variation of loads and the sporadic transient overloads pose additional computational difficulties and theoretical complexity. Limited materials data is another hurdle.

Although it was not within the scope of WPDIV to deal with all these non-trivial issues, an interim strategy had to be elaborated so that the design study could be started on a rational basis. Our approach includes following working categories:

- Creation of guidelines for a standard stress analysis procedure [75]
- Simulation-based modelling of possible or observed failure features [76-78]
- Formulation of dedicated failure criteria [79-81]
- Rule-based structural integrity assessment and verification [79-83]

In the WPDIV program, following topics were covered in order to fill the knowledge gaps:

1. Relative criticality of cyclic plasticity, fatigue and fast fracture (normal/off-normal operation)
2. Impact of inelastic stress relaxation during fabrication and operation (Cu, CuCrZr, W)
3. Impact of softening due to long-term thermal ageing (CuCrZr)
4. Impact of irradiation embrittlement and stress tri-axiality (Cu, CuCrZr, W)
5. Role of the singular stress/strain concentration at the material/geometrical discontinuities
6. Impact of local ratchetting on the global structural stability (Cu, CuCrZr)
7. Effect of recrystallization on the fatigue and cracking of the armour (W)

### 6.2. Mechanical response of the cassette [44]

During normal operation, the cassette experiences a pressure load (by pressurized coolant) and thermal load (by nuclear heating and radiation), which produces primary and secondary stresses, respectively. If a disruption occurs, the resulting electromagnetic force produces additional stress in the supports. These stresses could impair the mechanical integrity or eventually cause a structural failure if their intensity exceeds the specified critical limit. For a quantitative judgement on the risk of a potential failure mode, a proper calculation of stress fields is mandatory.
Fig. 33 shows the distribution of the equivalent (von Mises) stress in the CB and SL calculated for the thermal load (left) and the combined loads (right) assuming elasto-plastic behavior. It is seen that the resultant stress field under the combined loads is primarily due to the thermal stress field to a decisive degree while the static stress due to the coolant pressure has only a minor influence. The stress level (<250MPa) in the CB remains within the elastic regime whereas considerable stresses are produced in the SL. In a structural integrity assessment based on the elastic rules of RCC-MRx code, the fixing support of the SL was identified to be the most critical part due to relatively high temperature (~400°C) and the resulting thermal softening of EUROFER97 [74].
The radial displacement of the CB due to thermal expansion amounts to 8.4mm at the engaged outboard wishbone support (cf.: 10.1mm in an unconstrained state). The thermal stress produced in the wishbone by this thermal deformation amounts to locally up to 610MPa. However, this maximum stress is still lower than the yield stress of the titanium alloy applied for the wishbone.

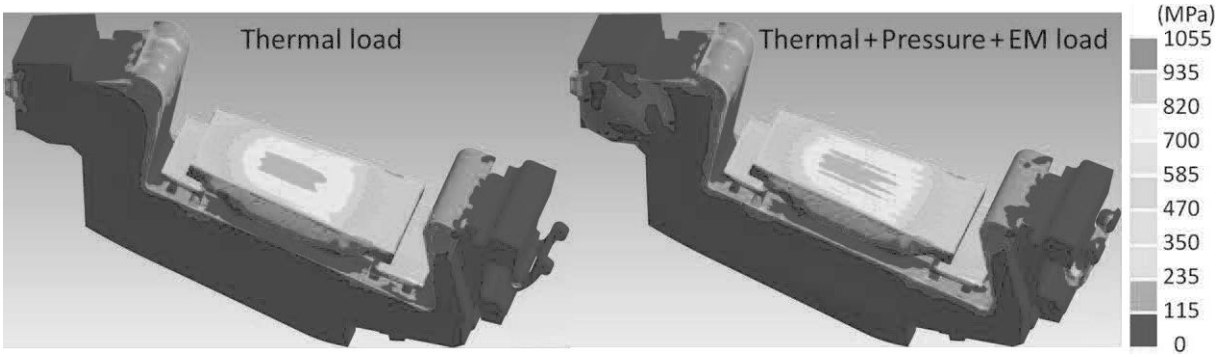

Fig. 33. Distribution of the equivalent (von Mises) stress in the CB and SL calculated for the thermal load and the combined loads (thermal, pressure and electromagnetic force) assuming the elasto-plastic material behavior.

6.3. Selected critical issues: electromagnetic impact loads [84]

In what follows, a few selected critical issues are highlighted.
The first case is the severe dynamic impact loads acting on the supports and the cooling pipework during a global plasma instability, e.g. disruption or vertical displacement event (VDE). This electromagnetic impact load is caused by the volumetric Lorentz force generated by the interaction between the total magnetic field (static plus excited) and the huge electric currents induced/injected in the conductive solid bodies as a consequence of the instability. Fig. 34 shows the transient time-history of the Lorentz forces resulting from a downward VDE. Owing to the fast transient process (current quench: 74ms, initiation of the eddy/halo current: 1.63s/1.66s) and the tremendous currents induced (total eddy current: 20MA, total halo current: 28kA), very acute and strong forces (cassette: ≤1.3MN, pipework: ≤130kN) and moments (cassette: ≤3.2MN·m, pipework: ≤315kN·m) are generated. The dynamic amplification of the initial loads by inertia effect must be taken into account. The impact loads can be drastically reduced if the supports between the cooling pipes and the VV are insulated (by 70%) or if the supports between the targets and the CB are insulated (by 96%).

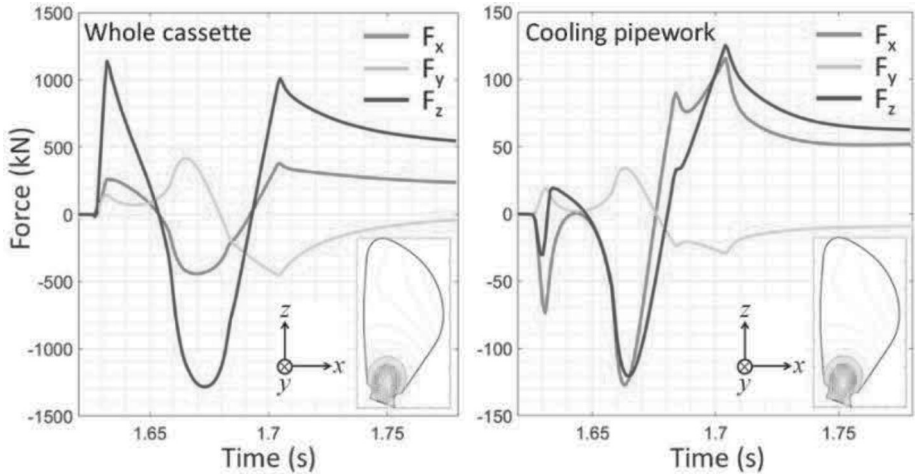

Fig. 34. Time-history of the Lorentz forces induced in the whole divertor (left) and in the cooling pipes (right) under a downward plasma vertical displacement event (1.67s after the onset of the instability).

6.4. Selected critical issues: uncertainty of stress states [59]

The initial stress state is coined as residual stress by the fabrication process. The extent of inelastic stress relaxation experienced thereby by the ductile constituents (copper interlayer and copper alloy cooling pipe) determines the actual residual stress. This process is difficult to simulate as the knowledge on the physical mechanism is limited and the required materials data (e.g. the parameters of primary creep) are often not available. As a consequence, it is very difficult to specify the effective stress free temperature

needed for stress calculation as reference (null strain) temperature. The effective stress free temperature has a decisive impact on stress calculation and failure modelling as manifested in Fig. 35.

Fig. 35 shows the stress variation at the front side target cooling pipe (hoop component in the cylindrical coordinate system) during a typical cyclic HHF loading (20MW/m²). The entire stress range moves from a compressive to tensile regime preserving the amplitude when the stress free temperature is shifted from 20°C to 580°C. Such a complete reversion of the stress sign will likely lead to a different failure behavior. Also the temporal offset between the cyclic phase of stress and temperature is dictated by the assumed stress free temperature. This response clearly indicates the direct impact of effective stress free temperature on the resulting residual stresses. To clarify this issue, a direct measurement of the residual stress was attempted by means of neutron diffractometry. This experimental tool enables calibration of the actual effective stress free temperature by fitting the computed stress profiles with measured ones. The diffraction data revealed that a substantial stress relaxation indeed occurred during fabrication [85]. A similar stress relaxation can also occur under the subsequent HHF loading as a consequence of creep or thermal ageing.

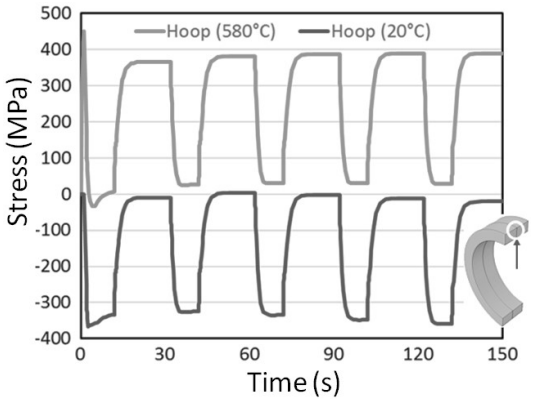


Fig. 35. Stress variation at the front side target cooling pipe (hoop stress in the cylindrical coordinate system) during the cyclic HHF loading (20MW/m²) after fabrication where two different effective stress free temperatures are assumed (red: 580°C, blue: 20°C) [59].

### 6.5. Selected critical issues: local damage concentration [59, 80]

The singular stress/strain concentration appearing at a material interface (particularly, at the free surface edge) is a characteristic feature of the monoblock-type targets and very difficult to handle. Fig. 36 shows the distribution of the strain range intensity (of the equivalent strain) in the upper part of the irradiated cooling pipe during a typical HHF loading cycle (10MW/m²) repeated between cooling (150°C) and heating. It is seen that the intensity of strain range is locally concentrated near the free surface edge of the bond interface. This singular strain concentration facilitates premature initiation of a fatigue crack. However, it is not clear whether this crack (if initiated at all) would really grow beyond the localized strain concentration region under the strain-controlled loading condition. Therefore, the term “number of cycles to fatigue failure” needs to be redefined more specifically noting the extent of crack growth, for instance, referring to either local (acceptable) or global (unacceptable) failure. Otherwise, a failure assessment dominated by the singular strain range will be burdened by an overly conservative criterion.

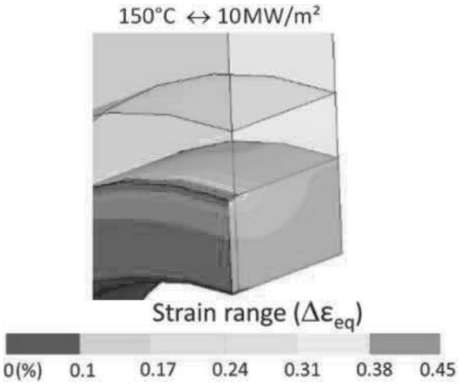

Fig. 36. Calculated strain range intensity in the upper part of the irradiated cooling pipe during a typical HHF loading cycle from cooling (150°C) to heating at 10MW/m².

6.6. Selected critical issues: exhaustion of ductility by irradiation [81]

Fig. 37 shows the ductility usage fraction in the lower part of the cooling pipe calculated for a HHF loading cycle at 20MW/m². The ductility usage fraction is defined as the ratio of the incremental strain used per each loading cycle to the limit strain estimated at each position based on the ultimate rupture strain, temperature, stress tri-axiality, irradiation dose (10dpa) and safety factor (e.g. 2). The normalized usage fraction values higher than unity means that the criterion is violated. Fig. 37 reveals that the usage fraction exceeds unity in the extensive region of the bottom area (critical hot spots: >3). This alarming result is attributed to the combined effect of embrittlement due to low-temperature irradiation (≤150°C) and the pronounced stress tri-axiality near the free edge of the bond interface. This failure risk presents a serious design concern (the criticality depends on code rules used). A fracture mechanics-based brittle failure criteria could be applied for handling the affected region. The quite high toughness of irradiated CuCrZr alloy seems to justify the design against fast fracture but needs further scrutiny.

On the other hand, the pronounced irradiation hardening of the initially ductile cooling pipe can have a beneficial effect against either plastic fatigue by decreasing the plastic strain range or stress intensity-based failures ($S_m$ or $3S_m$) by increasing yield stress. In this sense, irradiation effects are ambivalent [86].

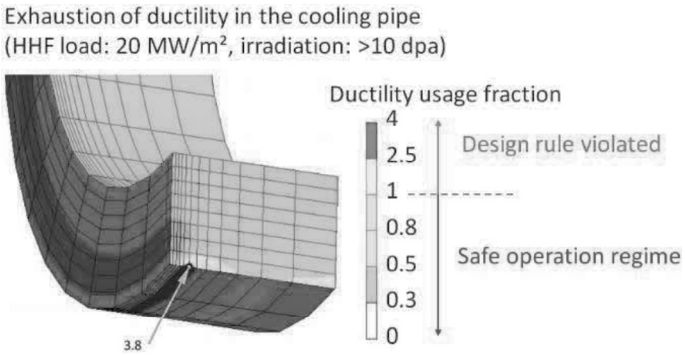

Fig. 37. Ductility usage fraction in the lower part of the cooling pipe calculated for the HHF loading cycle at 20MW/m² (cooling: 150°C) [81].

## 7. Technology

7.1. Technology issues and R&D topics

It is relevant to raise the question as to whether and to what extent the up-to-date ITER technologies are applicable or can be extrapolated for the DEMO divertor. To assess this question, the materials and the loading conditions specific for the divertors of the DEMO and ITER need to be compared. In Table 8, selected characteristics of the DEMO divertor are contrasted with the ITER divertor [7, 8, 87].

Table 8. Selected characteristics of the European DEMO divertor contrasted with the ITER divertor [7, 8, 87].

| | DEMO divertor | ITER divertor |
|---|---|---|
| Structural materials | CB: EUROFER97 steel<br>IVT/OVT: CuCrZr-IG alloy<br>SL: EUROFER97 steel | CB: SS 316 L(N)-IG/XM-19<br>IVT/OVT: CuCrZr-IG alloy<br>Dome: CuCrZr-IG alloy |
| Max. irradiation dose (dpa/fpy) | CB: 1 (target supports: 4)<br>SL (EUROFER97): 5<br>OVT: 2 (W), 7 (Cu) | CB: 0.1<br>Dome (Cu heat sink): 3.5<br>OVT: ≤0.5 (W), ≤2 (Cu) |
| Bulk nuclear heating (MW) | 133.4 | 101.6 |
| SOL conduction heat (MW) | 220 (incl. radiative dissipation) | 300 (incl. radiative dissipation) |
| Inlet temperature (water) | CB: 180°C, OVT: 130°C | CB: 100°C, OVT: 140°C |
| He production (appm/fpy) | SL (EUROFER97): 94<br>CB (EUROFER97): 49<br>OVT (Cu heat sink): 57 | Dome (Cu heat sink): 31<br>CB (316 L(N)): 2.5<br>OVT (Cu heat sink): 13 |
| Peak heat flux (MW/m²) | Steady state: 10 (2h)<br>Slow transient: 20 (10s) | Steady state: 10 (400s)<br>Slow transient: 20 (10s) |
| Transient events (assumed scenarios) | ELM: suppressed or mitigated<br>Disruptions: a few times only | ELM: suppressed or mitigated<br>Disruptions: a few times only |
| Lifetime (cycles/fpy) | 6500 (+ overhead)/1.5 | 3000/0.1 |

Table 8 suggests that the technologies of the ITER divertor (except for the targets) will not be applicable to the DEMO divertor because the main structural materials are essentially different from each other (austenitic vs. ferritic-martensitic steel). Moreover, the DEMO divertor is subject to much higher nuclear loads. This difference poses serious challenges with regard to design as well as technology.
Currently, the following topics are identified as major R&D objectives:

- Joining technologies for steel components (HIP, welding) and pipes (brazing)
- Manufacturing of medium-scale target mock-ups with the wire-reinforced composite pipe
- Coating of thick tungsten armour on a large steel plate (for SL)
- Anti-corrosion coating and corrosion-erosion test of the cooling pipe [88, 89]
- Coating for electrical insulation of the target supports
- Full-scale fabrication and hydraulic verification of the target pipework

In the PCD Phase, the R&D efforts were focused on the HHF technology whereas the R&D of the other subcomponents were shifted to the Concept Design (CD) Phase. This decision was mainly due to the facts that the design had not yet been fully detailed and very limited resources were available. As a consequence, in the baseline design, the aspect of overall technology feasibility was addressed only at a rudimentary level. In 2021, a comprehensive technology R&D program was launched for the entire cassette aiming at industrial manufacturability.

### 7.2. HHF Technology and performance [43, 90]

In the PCD, the approach was to take the HHF technology developed for ITER as working reference to take advantage of its maturity and availability, and to pursue evolutionary innovations for enhancing performances. The R&D program comprised concept studies (monoblock with a thermal break, flat-tile), novel materials (composite pipe, composite block, graded interlayer) and joining (hot radial pressing, hot isostatic pressing, brazing) [82, 83, 91-104]. All design variants were realized in form of a small-scale mock-up with the standard geometry and evaluated in an extensive and systematic HHF testing campaign using hydrogen neutral beam (20-25MW/m², 500-1000 pulses, 20-130°C coolant) and non-

destructive test inspection tools [105-111]. Selected examples of the design concepts are presented in Fig. 38.

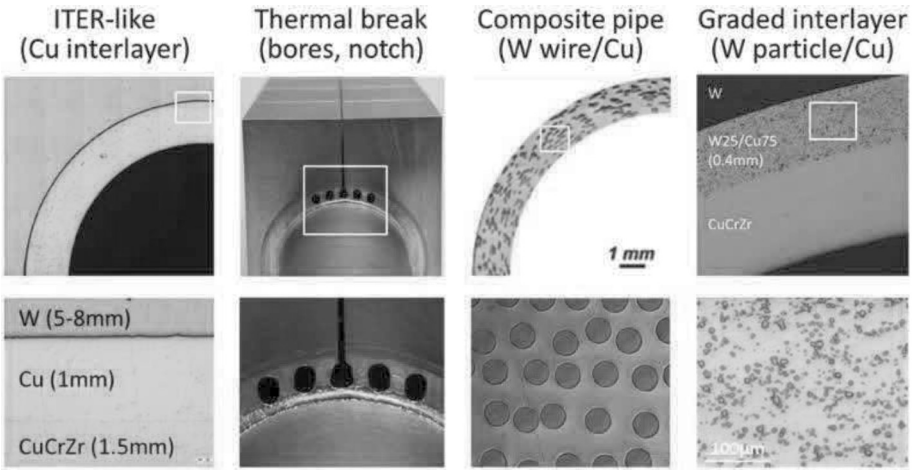


Fig. 38. Four selected monoblock-type design variants developed for the targets (fltr: ITER-like, thermal break, composite pipe, graded interlayer design concept)

The four monoblock-type variants (ITER-like, thermal break, composite pipe, graded interlayer) passed the qualification tests without any discernable indication of failure or deteriorated hear removal capacity. Moreover, the ITER-like baseline technology (joined by hot radial pressing) and the monoblock design with the tungsten wire-reinforced copper composite pipe (joined by brazing) showed an excellent HHF performance without any structural failure (albeit with armour surface damages) or indication of affected heat removal capacity even at 25MW/m² at least up to 500 pulses (coolant: 20°C). A stable heat removal performance without failure was demonstrated up to 32MW/m² (5 pulses) which was the physical limit nearly reaching the melting temperature of tungsten at the front face. The findings of the HHF tests are statistically reliable as supported by the large number of repeated test cases (290 monoblocks). Details of the technology R&D and the results of the HHF qualification tests are found elsewhere [43, 90].

Fig. 39 shows the in-situ infrared (IR) thermography images captured for the four target mock-ups under cyclic HHF loads at 20MW/m² up to 500 pulses (coolant: 130°C). The surface temperature distributions are compared between the first and the last pulse. The compared images display no significant change of temperature over the entire loading cycles indicating a sound structural integrity (note that the modest changes in color shading are due to the changing surface emissivity).

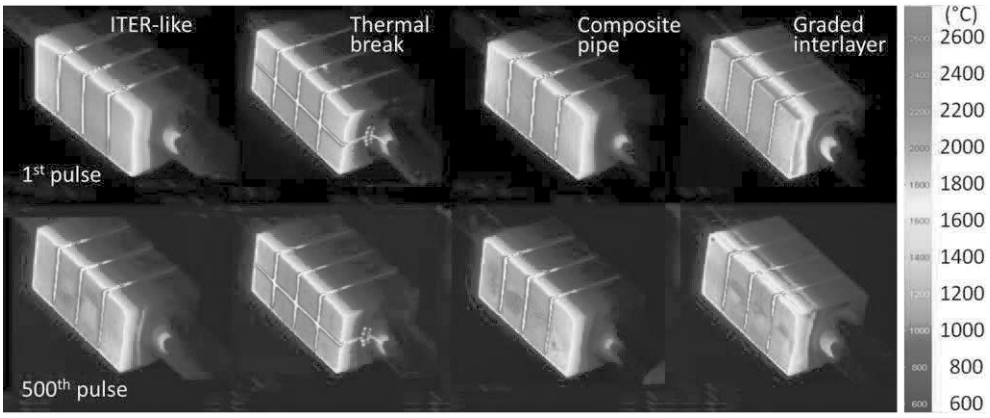


Fig. 39. In-situ infrared thermography (false color) images of the various monoblock-type target mock-ups (depicted in Fig. 38) under cyclic HHF loads at 20MW/m² up to 500 pulses (coolant: 130°C) [43].

Fig. 40 (a) shows the metallographic sections (axial cut) of two HHF-tested (20MW/m², 500 pulses) ITER-like target mock-ups each with the tungsten blocks produced by AT&M (left) or ALMT (right)

[43]. The photographs of the armour front faces loaded are also shown. Both micrographs reveal abnormal growth of recrystallized grains near the front face, but no single crack is seen on the cut sections as well as on the front faces. The ultrasonic inspection images (360° C-scan of reflected echo) presented in Fig. 40 (b) also confirm intact joining (except for the minor edge cracks in the AT&M blocks). The ITER-like and composite pipe monoblock mock-ups remained fully intact up to 1000 pulses at 20MW/m².

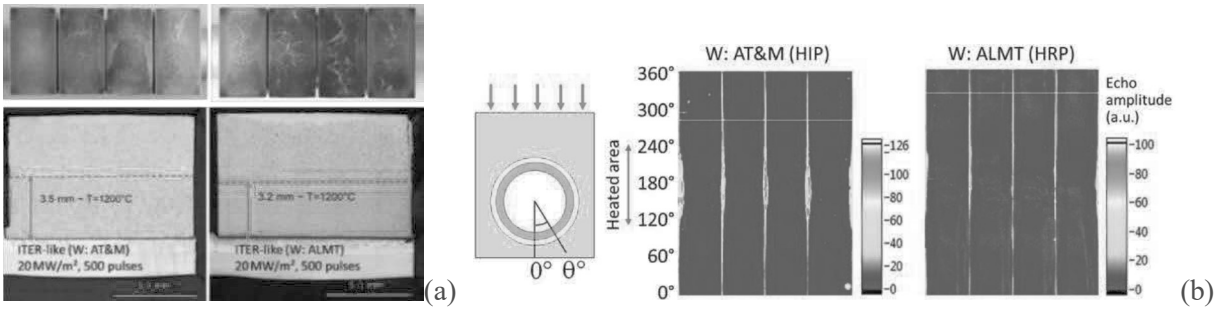


Fig. 40. (a) Metallographic sections (axial cut) of the HHF-tested (20MW/m², 500 pulses) ITER-like mock-ups with the tungsten blocks produced by AT&M (left) and ALMT (right), respectively, together with the photographs of the armour front faces, (b) Ultrasonic inspection images of the same mock-ups.

Fig. 41 (a) shows the front face photograph of the armour blocks (ITER-like target mock-up with AT&M tungsten) after 500 pulses at 25MW/m² and the laser profilometry image of a selected block revealing the topography of surface roughness. Severe surface damage due to visco-plastic straining is observed. The maximum height of roughness is 600µm. However, this mock-up sustained the damage maintaining an overall intact integrity except for a single tiny crack (see the metallographic cut sections in Fig. 41 (b) and withstood the HHF loads without any deterioration of heat removal capacity.

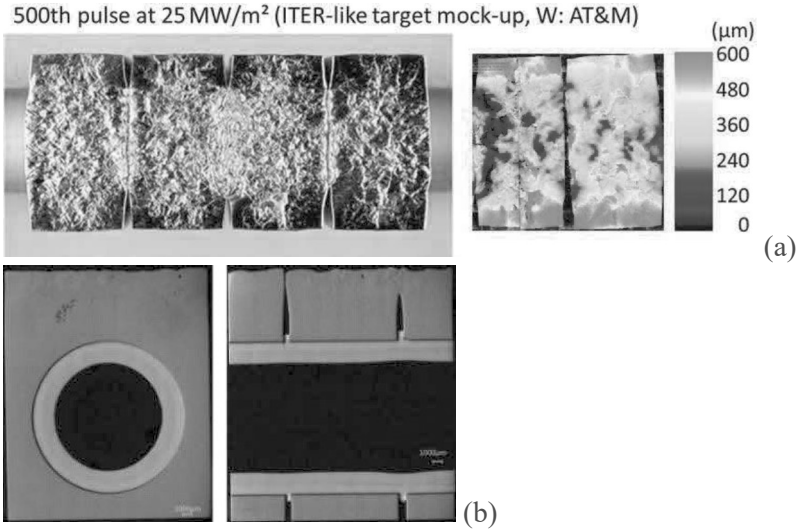


Fig. 41. (a) Photograph of the armour blocks (front face) of the ITER-like target mock-up after 500 HHF pulses at 25MW/m² and a laser profilometry image revealing surface roughness, (b) micrographs of the metallographic cut sections (transversal, axial).

## 8. Summary and Conclusions

In late 2020, the PCD for the European DEMO divertor has been concluded, delivering the baseline design after seven years of joint undertaking in the EUROfusion Consortium. To support the baseline design, comprehensive computational and experimental justifications were also delivered. The essential characteristics of the baseline design are as follows:

- Single-null magnetic configuration
- Modular cassette design to allow remote maintenance via the lower ports
- Shielding liner plate in lieu of a dome
- Minimized baffle area (in favor of increased breeding blanket area)
- Low-temperature water-cooling (OVT: 130°C, CB: 180°C) with two separate cooling circuits
- Reduced-activation (ferritic-martensitic) steel as major structural material
- Full tungsten targets based on the ITER-like high-heat-flux technology (monoblock-type armour)
- Direct integration of the targets onto the cassette body (no detachable plasma-facing unit)

The major achievements of the PCD are as follows:

- Delivery of the feasible (baseline) design concept with a preconceptual maturity
- Verification of the baseline design in terms of cooling, nuclear shielding and structural integrity
- Formulation of the inelastic structural integrity assessment procedure where guidelines for structural analysis, failure criteria (tailored for the ITER-like target) and case studies are presented
- Full-scale experimental verification of the hydraulics performance of the target cooling circuit
- Demonstration of high-quality fabrication and excellent HHF performance of the target technologies
- Comparative assessment of the reliability and detection limit of nondestructive inspection methods
- Demonstration of the fit-for-purpose for the neutron diffractometry and tomography imaging of the small-scale target mock-ups for measuring residual stress and for detecting internal defects.
- Qualitative demonstration of the anti-corrosion performance of a protective coating on the pipe wall tested in a water-loop with controlled water chemistry and flow condition.

The key findings and open issues from the PCD are:

- The lifetime of the divertor (1.5fpy) is primarily limited by the irradiation damage of the steel at the nuclear hot spots rather than the armour erosion rate (if ELM is fully suppressed).
- Nuclear transmutation produces a high concentration of helium in the CB and SL, particularly, near the front face (≤140appm after 1.5fpy). The considerable He concentration raises the potential issue of reduced lifetime and limited recyclability of the steel components (stable He bubbles can be removed only by melting).
- Even with the low coolant temperature of the cassette body approaching the acceptable lower limit specified for irradiated EUROFER97 steel, the margin to the critical heat flux is still tight or even locally exhausted (higher pressure is required).
- The state-of-the-art HHF technology based on the tungsten monoblock-type design has demonstrated an excellent heat removal capacity and highly reliable fatigue resistance under the DEMO-relevant HHF loads up to 25MW/m² in thermal equilibrium.
- The HHF performance of the monoblock-type target designs seems to fulfill the design requirements from both the thermo-hydraulic and structure-mechanical point of view.
- The front face layer of the plasma-facing components (targets, shielding liner) are directly exposed to intense neutron fluxes experiencing excessive nuclear loads (lattice damage and transmutation).
- The divertor design comprises many complex geometrical entities featuring numerous discontinuities and joints. These discontinuities and joining interfaces (e.g. weld seam, brazes, diffusion bonds) tend to act as stress concentrators susceptible to irradiation embrittlement and prone to cracking.
- The structural reliability of the steel structures could not be fully assessed because required materials data from relevant irradiation tests ($T_{irr}$≤150-200°C) are missing (will be available in the early Engineering Design Phase).
- Further critical issues are: rationalized design of supports for straightforward on-site remote handling, precision production for keeping fabrication allowance, resilience for contingency (e.g. disruption).

## 9. Outlook

In the CD Phase (2021-2027), the main focus of the project efforts shall be placed on:

1. An alternative design concept for the cassette which allows easier remote handling (particularly, to enable on-site replacement of the PFCs) and reduced maintenance downtime (via a reduced number of the feeding pipes). To this end, a fully revised design with a single cooling circuit and a simplified target attachment design will be elaborated.
2. Rigorous structure-mechanical assessment to ensure the structural integrity and reliability of the steel structures to be irradiated below the DBTT. For supporting this, a dedicated modelling methodology and proper failure criteria with a balanced conservativism shall be formulated.
3. Launching of the preliminary technology R&D program to explore industrial manufacturability of the major steel structures and ancillary components (pipework, supports, armour, etc).
4. Further maturation of HHF technology with innovative technical approaches (e.g. joining, composite cooling pipe, anti-corrosion coating, etc.) including medium-scale prototype fabrication and HHF verification.

## Acknowledgement

This work has been carried out within the framework of the EUROfusion Consortium and has received funding from the Euratom research and training program 2014-2018 and 2019-2020 under grant agreement No 633053. The views and opinions expressed herein do not necessarily reflect those of the European Commission.
The authors (particularly, JHY as the Project leader) are very grateful to the WPDIV Design Review Panel (chair: D. Stork, members: A. Cardella, C. Ibbott, R. Tivey) for their valuable recommendations and constructive (and fair) criticisms from their rich experiences. In addition, JHY wants to thank the PPPT department head (G. Federici) and his team for their supports and guidance. Finally, the authors appreciate all the contributions from the previous members of the WPDIV.

## References

[1] G. Federici et al., Overview of the design approach and prioritization of R&D activities towards an EU DEMO, Fusion Eng. Des. 109-111 (2016) 1464-1474.

[2] G. Federici et al., DEMO Design Activity in Europe: Progress and Updates, Fusion Eng. Des. 136 (2018) 729-741.

[3] J.H. You et al., Conceptual design studies for the European DEMO divertor: Rationale and first results, Fusion Eng. Des. 109-111 (2016) 1598-1603.

[4] J.H. You et al., Progress in the initial design activities for the European DEMO divertor: Subproject Cassette, Fusion Eng. Des. 124 (2017) 364-370.

[5] D. Marzullo et al., Systems engineering approach for pre-conceptual design of DEMO divertor cassette, Fusion Eng. Des. 124 (2017) 649-654.

[6] F. Crescenzi et al., ITER-like divertor target for DEMO: Design study and fabrication test, Fusion Eng. Des. 124 (2017) 432-436.

[7] R. Tivey et al., ITER divertor, design issues and research and development, Fusion Eng. Des. 46 (1999) 207-220.

[8] A.S. Kukushkin et al., Divertor issues on ITER and extrapolation to reactors, Fusion Eng. Des. 65 (2003) 355-366.

[9] M. Turnyanskiy et al., A roadmap to the realization of fusion energy: mission for solution on heat-exhaust systems, Fusion Eng. Des. 96-97 (2015) 361-364.

[10] C. Bachmann et al., Issues and strategies for DEMO in-vessel component integration, Fusion Eng. Des. 112 (2016) 527-534. (small divertor, no PFU)

[11] G. Federici et al., European DEMO design strategy and consequences for materials, Nucl. Fusion 57 (2017) 092002.

[12] H. Reimerdes et al., Assessment of alternative divertor configurations as an exhaust solution for DEMO, Nucl. Fusion 60 (2020) 066030.

[13] G. Federici et al., Magnetic Confinement Fusion-Technology-Fusion Core, Encyclopedia of Nuclear Energy, Elsevier (2021) 554-575. https://doi.org/10.1016/B978-0-12-819725-7.00050-7

[14] U. Bonavolontà et al., EU-DEMO divertor: Cassette design and PFCs integration at pre-conceptual stage, Fusion Eng. Des. 159 (2020) 111784.

[15] G. Mazzone et al., Eurofusion-DEMO Divertor - Cassette Design and Integration, Fusion Eng. Des. 157 (2020) 111656.

[16] J. Wesson, Tokamaks (Oxford Engineering Science Series, 48), Oxford University Press; 2. Ed. ISBN-10: 0198562934 (1997).

[17] N. Asakura et al., Plasma Exhaust and Divertor Studies in Japan and Europe Broader Approach, DEMO Design Activity, Fusion Eng. Des. 136 (2018) 1214-1220.

[18] M. Siccinio et al., Figure of merit for divertor protection in the preliminary design of the EU-DEMO reactor, Nucl. Fusion 59 (2019) 106026.

[19] N. Asakura et al., Power Exhaust Studies and Divertor Designs for Japanese and European DEMO Fusion Reactors, Nucl. Fusion, submitted.

[20] A. Loarte et al, Power exhaust in tokamaks and scenario integration issues, Fusion Eng. Des. 122 (2017) 256-273.

[21] J.H. You et al., Nuclear loads and nuclear shielding performance of EU DEMO divertor: A preliminary neutronics evaluation of two interim design options, Nucl. Mater. Ener. 23 (2020) 100745.

[22] C. Day et al., DEMO Tritium fueling and vacuum systems, Fusion Eng. Des., this issue.

[23] C. Gliss, Integrated design of the DEMO lower ports, Eurofusion report 2MSRLH (2020).

[24] I.E. Garkusha et al., Performance of deformed tungsten under ELM-like plasma exposures in QSPA Kh-50, J. Nucl. Mater. 415 (2011) S65-S69.

[25] G. Federici et al., Overview of the DEMO staged design approach in Europe, Nucl. Fusion 59 (2019) 066013.

[26] R. Kembleton et al., Benefits and challenges of advanced divertor configurations in DEMO, Fusion Eng. Des., this issue.

[27] P. Rindt et al., Conceptual design of a liquid-metal divertor for the European DEMO, Fusion Eng. Des. In press.

[28] M. Zhao et al., CFD evaluation and optimization of the HEMJ divertor cooling design, Fusion Eng. Des. 158 (2020) 111669.

[29] W. Wen et al., Heat pipe technology based divertor plasma facing component concept for European DEMO, Fusion Eng. Des. 164 (2021) 112184.

[30] C. Bachmann, Plant Description Document (v. 1.9), Eurofusion report (2021) 2KVWQZ.

[31] F. Cismondi et al., Progress in EU-DEMO In-Vessel Components integration, Fusion Eng. Des. 124 (2017) 562-566.

[32] T. Pinna et al., Safety important classification of EU DEMO components, Fusion Eng. Des. 146 (2019) 631-636.

[33] D. Marzullo et al., Progress in the pre-conceptual CAD engineering of European DEMO divertor cassette, Fusion Eng. Des. 146 (2019) 942-945.

[34] D. Marzullo, CAD Design - 2nd phase, Eurofusion report (2020) 2NL4LT.

[35] M. Rieth et al., EUROFER 97 Tensile, Charpy, Creep and Structural Tests, Forschungszentrum Karlsruhe Wissenschaftliche Berichte FZKA 6911 (2003).

[36] G. Mazzone et al., Structural verification and manufacturing procedures of the cooling system for DEMO divertor target (OVT), Fusion Eng. Des. 146 (2019) 1610-1614.

[37] V. Imbriani et al., Insulated fixation system of plasma facing components to the divertor cassette in Eurofusion-DEMO, Fusion Eng. Des. 158 (2020) 111710.

[38] T. Hirai et al., ITER tungsten divertor design development and qualification program, Fusion Eng. Des. 88 (2013) 1798-1801.

[39] M. Li et al., Interpretation of the deep cracking phenomenon of tungsten monoblock targets observed in high-heat-flux fatigue tests at 20 MW/m², Fusion Eng. Des. 101 (2015) 1-8.

[40] M. Li et al., Design options to mitigate deep cracking of tungsten armor, Fusion Eng. Des. 124 (2017) 468-472.

[41] M. Li et al., Structural impact of armor monoblock dimensions on the failure behavior of ITER-type divertor target components: Size matters, Fusion Eng. Des. 113 (2016) 162-170.

[42] M. Li et al., Fracture mechanical analysis of a tungsten monoblock-type plasma-facing component without macroscopic interlayer for high-heat-flux divertor target, Fusion Eng. Des. 122 (2017) 124-130.

[43] J. H. You et al., High-heat-flux technologies for the European demo divertor targets: State-of-the-art and a review of the latest testing campaign, J. Nucl. Mater. 544 (2021) 152670.

[44] P. Frosi, Loads specification and structural analysis, Eurofusion report 2P8PER (2020).

[45] R.A. Kempf et al., Correlation between radiation damage and magnetic properties in reactor vessel steels, J. Nucl. Mater. 445 (2014) 57-62.

[46] R. Villari et al, Annex to Loads Specification (LS) for divertor cassette and PFCs: Neutronic analysis of DEMO divertor 2019, Eurofusion report 2NL3S8 (2020).

[47] P.A. Di Maio et al., Thermal-hydraulic study of the DEMO divertor cassette body cooling circuit equipped with a liner and two reflector plates, Fusion Eng. Des. 167 (2021) 112227.

[48] P. A. Di Maio et al., Computational thermofluid-dynamic analysis of DEMO divertor cassette body cooling circuit, Fusion Eng. Des. 136 (2018) 1588-1592.

[49] P. A. Di Maio et al., On the thermal-hydraulic optimization of DEMO divertor plasma facing components cooling circuit, Fusion Eng. Des. 136 (2018) 1438-1443.

[50] P. A. Di Maio et al., Thermal-hydraulic optimisation of the DEMO divertor cassette body cooling circuit equipped with a liner, Fusion Engineering and Design 146 (2019) 220-223.

[51] P. A. Di Maio et al., Hydraulic analysis of EU-DEMO divertor plasma facing components cooling circuit under nominal operating scenarios, Fusion Engineering and Design 146 (2019) 1764-1768.

[52] P.A. Di Maio et al., On the thermal-hydraulic performances of the DEMO divertor cassette body cooling circuit equipped with a liner, Fusion Eng. Des. 156 (2020) 111613.

[53] P.A. Di Maio et al., On the numerical assessment of the thermal-hydraulic operating map of the DEMO divertor plasma facing components cooling circuit, Fusion Eng. Des. 161 (2020) 111919.

[54] P.A. Di Maio et al., Hydraulic assessment of an upgraded pipework arrangement for the DEMO divertor plasma facing components cooling circuit, Fusion Eng. Des. 168 (2021) 112368.

[55] J. H. You et al., European DEMO divertor target: Operational requirements and material-design interface, Nucl. Mater. Ener. 9 (2016) 171-176.

[56] S.A. Fabritsiev et al., Low-temperature radiation embrittlement of copper alloys, J. Nucl. Mater. 233-237 (1996) 513-518.

[57] G.M. Kalinin et al., The effect of irradiation on tensile properties and fracture toughness of CuCrZr and CuCrNiSi alloys, J. Nucl. Mater. 417 (2011) 908-911.

[58] S. Tähtinen et al., Effect of neutron irradiation on fracture toughness behavior of copper alloys, J. Nucl. Mater. 258-263 (1998) 1010-1014.

[59] J. H. You et al., Structural lifetime assessment for the DEMO divertor targets: Design-by-analysis approach and outstanding issues, Fusion Eng. Des. 164 (2021) 112203.

[60] J.H. You, Copper matrix composites as heat sink materials for water-cooled divertor target, Nucl. Mater. Ener. 5 (2015) 7-18.

[61] J.H. You, A review on two previous divertor target concepts for DEMO: Mutual impact between structural design requirements and materials performance, Nucl. Fusion 55 (2015) 113026.

[62] E. Gaganidze et al., Assessment of neutron irradiation effects on RAFM steels, Fusion Eng. Des. 88 (2013) 118-128.

[63] G. Mazzone et al., Choice of a low operating temperature for the DEMO EUROFER97 divertor cassette, Fusion Eng. Des. 124 (2017) 655-658.

[64] DEMO design criteria for in-vessel components (DDC-IC) Part-B: Design criteria and analysis procedures, first draft (2020).

[65] B. van der Schaaf et al., The development of EUROFER reduced activation steel, Fusion Eng. Des. 69 (2003) 197-203.

[66] S. Noce et al., Neutronics analysis and activation calculation for Tungsten used in the DEMO divertor targets: A comparative study between the effects of WCLL and HCPB blanket, different W compositions and Chromium, Fusion Eng. Des. 169 (2021) 112428.

[67] S. Noce et al., Nuclear analyses for the design of the ITER-like plasma facing components vertical targets of the DEMO divertor, Fusion Eng. Des. 155 (2020) 111730.

[68] S.A. Fabritsiev et al., Neutron irradiation induced high temperature embrittlement of pure copper, Plas. Dev. Oper. 5 (1997) 133-141.

[69] RCC-MRx 2018 AFCEN edition, Design and construction rules for mechanical components of nuclear installation.

[70] ITER Structural Design Criteria for In-vessel Components, G 74 MA 8 01-05-28 W0.2.

[71] P. Frosi et al., Structural design of DEMO Divertor Cassette Body: FEM analysis and introductive application of RCC-MRx design rules, Fusion Eng. Des. 109-111 (2016) 47-51.

[72] P. Frosi et al., Structural analysis of DEMO divertor cassette body and design study based on RCC-MRx, Fusion Eng. Des. 124 (2017) 628-632.

[73] P. Frosi et al., Further improvements in the structural analysis of DEMO Divertor Cassette body and design assessment according to RCC-MRx, Fusion Eng. Des. 138 (2019) 119-124.

[74] P. Frosi et al., DEMO Divertor shielding components assessment according to RCC-MRx, Fusion Eng. Des., submitted.

[75] M. Fursdon et al., An elastic analysis procedure for assessing divertor monoblock designs, Fusion Eng. Des. 135 (2018) 154-164.

[76] M. Li et al., Fracture mechanical analysis of tungsten armor failure of a water-cooled divertor target, Fusion Eng. Des. 89 (2014) 2716-2725.

[77] M. Li et al., Low cycle fatigue behavior of ITER-like divertor target under DEMO-relevant operation conditions, Fusion Eng. Des. 90 (2015) 88-96.

[78] M. Li et al., Structural impact of creep in tungsten monoblock divertor target at 20 MW/m², Nucl. Mater. Ener. 14 (2018) 1-7.

[79] M. Fursdon et al., Enhancements in the structural integrity assessment of plasma facing components, Fusion Eng. Des. 146 B (2019) 1591-1595.

[80] M. Fursdon et al., Towards reliable design-by-analysis for divertor plasma facing components - guidelines for inelastic assessment (part I: unirradiated), Fusion Eng. Des. 147 (2019) 111234.

[81] M. Fursdon et al., Towards reliable design-by-analysis for divertor plasma facing components - Guidelines for inelastic assessment (part II: irradiated), Fusion Eng. Des. 160 (2020) 111831.

[82] F. Crescenzi et al., FEM and thermal fatigue testing comparison of ITER-like divertor PFUs mock-ups for DEMO, Fusion Eng. Des. 136 (2018) 558-562.

[83] F. Domptail et al., The design and optimization of a monoblock divertor target for DEMO using thermal break interlayer, Fusion Eng. Des. 154 (2020) 111497.

[84] G. Di Mambro et al., Mechanical impact of electromagnetic transients on the European DEMO divertor. Part 1: Vertical Displacement Event, Fusion Eng. Des. submitted.

[85] R. Coppola et al., Neutron diffraction measurement of residual stresses in an ITER like tungsten-monoblock type plasma-facing component, Fusion Eng. Des. 146 (2019) 701-704.

[86] V. Barabash et al., Specification of CuCrZr alloy properties after various thermo-mechanical treatments and design allowables including neutron irradiation effects, J. Nucl. Mater. 417 (2011) 904-907.

[87] M. Merola et al., Engineering challenges and development of the ITER Blanket System and Divertor, Fusion Eng. Des. 96–97 (2015) 34-41.

[88] J. Öijerholm et al., Assessment of Flow-Accelerated Corrosion Rate of Copper Alloy Cooling Tube for Application in Fusion Reactors, Proc. Int. Conf. Water Chemistry in Nuclear Reactor Systems (2021).

[89] C. Harrington et al., Target cooling pipe corrosion-erosion protection technology, Eurofusion report 2NECDY (2020).

[90] J. H. You et al., European divertor target concepts for DEMO: Design rationales and high heat flux performance, Nucl. Mater. & Ener. 16 (2018) 1-11.

[91] F. Crescenzi et al., Design optimization of the DEMO ITER-like water-cooled divertor, Fusion Engineering and Design 98-99 (2015) 1263-1266.

[92] E. Visca et al., Manufacturing and testing of ITER-like divertor plasma facing mock-ups for DEMO, Fusion Eng. Des. 136 (2018) 1593-1596.

[93] Th. Barrett et al., Progress in the engineering design and assessment of the European DEMO first wall and divertor plasma facing components, Fusion Engineering and Design 109-111 (2016) 917-924.

[94] M. Fursdon et al., The development and testing of the thermal-break divertor monoblock target design delivering 20MW/m2 heat load capability, Phys. Scr. T170 (2017) 014042 (7pp).

[95] A. Lukenskas et al., High heat flux test results for a thermal break DEMO divertor target and subsequent design and manufacture development, Fusion Eng. Des. 146 (2019) 1657-1660.

[96] A. v. Müller et al., Melt infiltrated W-Cu composites as advanced heat sink materials for plasma facing components of future nuclear fusion devices, Fusion Eng. Des. 124 (2017) 455-459.

[97] A. v. Müller et al., Application of tungsten-copper composite heat sink materials to plasma-facing component mock-ups, Phys. Scr. T171 (2020) 014015 (8pp).

[98] E. Tejado et al., Evolution of mechanical performance with temperature of W/Cu and W/CuCrZr composites for fusion heat sink applications, Mater. Sci. Eng. A 712 (2018) 738-746.

[99] E. Tejado et al., The thermo-mechanical behaviour of W-Cu metal matrix composites for fusion heat sink applications: The influence of the Cu content, J. Nucl. Materi. 498 (2018) 468-475.

[100] J.H. You et al., Thermal and mechanical properties of infiltrated W/CuCrZr composite materials for functionally graded heat sink application, Journal of Nuclear Materials 438 (2013) 1-6.

[101] M. Richou et al., Realization of high heat flux tungsten monoblock type target with graded interlayer for application to DEMO divertor, Phys. Scr. T170 (2017) 014022 (7pp).

[102] M. Richou et al., Status on the W monoblock type high heat flux target with graded interlayer for application to DEMO divertor, Fusion Eng. Des. 124 (2017) 338-343.

[103] M. Richou et al., Performance assessment of high heat flux W monoblock type target using thin graded and copper interlayers for application to DEMO divertor, Fusion Eng. Des. 146 (2019) 858-861.

[104] M. Richou et al., Performance assessment of thick W/Cu graded interlayer for DEMO divertor target, Fusion Eng. Des. 157 (2020) 111610.

[105] F. Gallay et al., Quantitative thermal imperfection definition using non-destructive infrared thermography on an advanced DEMO divertor concept, Phys. Scr. T170 (2017) 014015 (5pp).

[106] G. Dose et al., Ultrasonic analysis of tungsten monoblock divertor mock-ups after high heat flux test, Fusion Eng. Des. 146 (2019) 870-873.

[107] S. Roccella et al., Ultrasonic test results before and after high heat flux testing on W-monoblock mock-ups of EU-DEMO vertical target, Fusion Eng. Des. 160 (2020) 111886.

[108] Y. Addab et al., Typology of defects in DEMO divertor target mockups, Phys. Scr. submitted.

[109] T. Minniti et al., Structural integrity of DEMO divertor target assessed by neutron tomography, Fusion Eng. Des. 169 (2021) 112661.

[110] H. Greuner et al., Progress in high heat flux testing of European DEMO divertor mock-ups, Fusion Eng. Des. 146 (2019) 216-219.

[111] H. Greuner et al., Assessment of the high heat flux performance of European DEMO divertor mock-ups, Phys. Scr. T171 (2020) 014003 (7pp).